

Observations of the [C I] ($^3P_1-^3P_0$) emission toward the massive star-forming region RCW38: further evidence for highly-clumped density distribution of the molecular gas

Natsuko Izumi,^{1,2,3,*} Yasuo Fukui,⁴ Kengo Tachihara,⁴ Shinji Fujita,⁵ Kazufumi Torii,⁶ Takeshi Kamazaki,² Hiroyuki Kaneko,^{7,2} Andrea Silva,² Daisuke Iono,² Munetake Momose,¹ Kanako Sugimoto,² Takeshi Nakazato,² George Kosugi,² Jun Maekawa,² Shigeru Takahashi,⁶ Akira Yoshino,² and Shin'ichiro Asayama²

¹College of Science, Ibaraki University, 2-1-1 Bunkyo, Mito, Ibaraki 310-8512, Japan

²National Astronomical Observatory of Japan, National Institutes of Natural Sciences, 2-21-1 Osawa, Mitaka, Tokyo 181-8588, Japan

³Institute of Astronomy and Astrophysics, Academia Sinica, No. 1, Section 4, Roosevelt Road, Taipei 10617, Taiwan

⁴Department of Physics, Nagoya University, Chikusa-ku, Nagoya, Aichi 464-8601, Japan

⁵Department of Physical Science, Graduate School of Science, Osaka Prefecture University, 1-1 Gakuen-cho, Naka-ku, Sakai, Osaka 599-8531, Japan

⁶Nobeyama Radio Observatory, National Astronomical Observatory of Japan (NAOJ), National Institutes of Natural Sciences (NINS), 462-2 Nobeyama, Minamimaki, Minamisaku-gun, Nagano 384-1305, Japan

⁷Graduate School of Education, Joetsu University of Education, 1 Yamayashiki-machi, Joetsu, Niigata, 943-8512, Japan

*E-mail: nizumi923@gmail.com

Received (2020 June 1); Accepted (2020 December 1)

Abstract

We present observations of the $^3P_1-^3P_0$ fine-structure line of atomic carbon using the ASTE 10 m sub-mm telescope towards RCW38, the youngest super star cluster in the Milky Way. The detected [C I] emission is compared with the CO $J = 1-0$ image cube presented in Fukui et al. (2016) which has an angular resolution of $40''$ (~ 0.33 pc). The overall distribution of the [C I] emission in this cluster is similar to that of the ^{13}CO emission. The optical depth of the [C I] emission was found to be $\tau = 0.1-0.6$, suggesting mostly optically thin emission. An empirical conversion factor from the [C I] integrated intensity to the H_2 column density was estimated as $X_{[\text{C I}]} = 6.3 \times 10^{20} \text{ cm}^{-2} \text{ K}^{-1} \text{ km}^{-1} \text{ s}$ (for visual extinction: $A_V \leq 10$ mag) and $1.4 \times 10^{21} \text{ cm}^{-2} \text{ K}^{-1} \text{ km}^{-1} \text{ s}$ (for A_V of 10–100 mag). The column density ratio of the [C I] to CO ($N_{[\text{C I}]} / N_{\text{CO}}$) was derived as ~ 0.1 for A_V of 10–100 mag, which is consistent with that of the Orion cloud presented in Ikeda et al. (2002). However, our results cover an A_V regime of up to 100 mag, which is wider than the coverage found in Orion, which reach up to ~ 60 mag. Such a high [C I]/CO ratio in a high A_V region is difficult to be explained by the plane-parallel photodissociation region (PDR) model, which predicts that this ratio is close to 0 due to the

heavy shielding of the ultraviolet (UV) radiation. Our results suggest that the molecular gas in this cluster is highly clumpy, allowing deep penetration of UV radiation even at averaged A_V values of 100 mag. Recent theoretical works have presented models consistent with such clumped gas distribution with a sub-pc clump size (e.g., Tachihara et al. 2018).

Key words: ISM: clouds — ISM: massive star-forming region — photon-dominated region (PDR)

1 Introduction

Interstellar molecular clouds are the site of star formation in galaxies. Ultraviolet (UV) photons emitted from OB-stars have significantly influence the structure and chemical diversity of the molecular clouds, and the behavior of ionized regions within them has been of great interest in the last decades (e.g., Hollenbach & Tielens 1997). A partially ionized layer in a molecular cloud faced to UV photons is known as a “photodissociation region (PDR)” and its structure has been intensively studied theoretically (e.g., Tielens & Hollenbach 1985; Hollenbach et al. 1991). The plane-parallel model (e.g., Hollenbach & Tielens 1999) of a PDR suggests that these regions comprise layers with different chemical abundances such as, H/H₂ and C⁺/C/CO, in the order of the ionization/dissociation energy where relatively uniform density distribution was assumed. This model predicts the concentration of atomic carbon in a visual extinction (A_V) range of 3–6 mag (e.g., Tielens & Hollenbach 1985; van Dishoeck & Black 1988; Hollenbach et al. 1991). The PDR theory must be observationally tested to understand the physics and chemistry in PDRs better. In particular, atomic carbon lies in the intermediate layer next to CO, and its transitions can provide for a sensitive probe of the carbon chemistry in PDRs. After the pioneering studies (e.g., Phillips et al. 1980; Keene et al. 1985), the 3P_1 – 3P_0 fine-structure line of atomic carbon [CI] (492.16967 GHz) has been known to be a good tracer of interstellar atomic carbon. Past observations have revealed that [CI] coexists with CO and their intensities correlate with each other. Large-area [CI] mapping observations toward the Galactic plane with low-UV ($G_0 \sim 1.7$ – 5.1 : typical average interstellar value) have shown that the distribution of the [CI] emission is almost similar to that of the CO emission (e.g., Oka et al. 2005; Burton et al. 2015). [CI] observations in regions with intense UV radiation also show that the [CI] and CO distributions of Orion and Carina clouds are similar to each other, where G_0 is 10^4 – 10^5 (e.g. Ikeda et al. 2002; Kramer et al. 2008; Shimajiri et al. 2013). Shimajiri et al. (2013) performed [CI] mapping observations at a resolution of $21''.3$ (~ 0.04 pc) toward the Orion A cloud with the Atacama Submillimeter Telescope Experiment (ASTE)

10 m telescope. They found that [CI] shows a similar distribution than ^{13}CO and did not find a layer of [CI] outside the ^{13}CO distribution. These observations indicate that the [CI] distribution is similar to CO distribution, suggesting that the plane-parallel PDR model presented in the early works may not be appropriate for molecular clouds. Therefore, this model must be tested by analyzing the behavior of [CI] in more PDR samples.

RCW38 (Rodgers et al. 1960) is an HII region of intense UV radiation located at a relatively small distance of 1.7 kpc from the Sun. It contains ~ 20 candidate O-stars, slightly larger than in the Orion KL region, in a volume of less than 1 pc (Wolk et al. 2006) and is very luminous with $L \sim 7 \times 10^5 L_\odot$ (Furniss et al. 1975). This source is, therefore, ideal to test the PDR model. There are two remarkable infrared peaks in the central part of RCW38 (Frogel, & Persson 1974). The brightest $2.2 \mu\text{m}$ source is labeled as IRS 2, and corresponds to a O5.5 binary system (DeRose et al. 2009). The brightest $10 \mu\text{m}$ feature located 0.1 pc west of IRS 2 is labeled as IRS 1. This is a dust ridge extending for 0.1–0.2 pc in the north–south direction (Smith et al. 1999). Furthermore, RCW38 is the youngest super star cluster in the Galaxy ($\lesssim 1$ Myr; e.g., Wolk et al. 2006; Wolk et al. 2008; Winston et al. 2011).

Molecular clouds were observed by Zinchenko et al. (1995) in the central region of RCW38 in the CS emission (resolution: $\sim 1'$) to resolve the ring-like shape surrounding the O-star candidates. Yamaguchi et al. (1999) observed a large area of RCW38 in the $^{13}\text{CO}(1-0)$ emission with the NANTEN 4 m telescope at a lower resolution ($2'.7$) and found an extended molecular cloud surrounding the HII region. Gyulbudaghian, & May (2008) performed $^{12}\text{CO}(1-0)$ observation with the SEST telescope at $45''$ resolution for a small $160'' \times 160''$ region. The $^{12}\text{CO}(1-0)$ emission shows two different velocity components at -3 – 2 km s⁻¹ and 3 – 8 km s⁻¹. Recently, Fukui et al. (2016) conducted observations of $^{12}\text{CO}(1-0)$, $^{13}\text{CO}(1-0)$, C¹⁸O(1-0), and $^{12}\text{CO}(3-2)$ toward RCW38 with Mopra, ASTE, and NANTEN2 telescopes. The observations revealed detailed distributions of two molecular clouds at the velocities of 2 and 14 km s⁻¹ toward RCW38. The Ring cloud (the 2 km s⁻¹ cloud) exhibits a ring-like shape with a cavity ionized by the cluster and has a high H₂ column density of $\sim 10^{23}$

cm^{-2} , whereas, the Finger cloud (the 14 km s^{-1} cloud) has a tip toward the cluster and has a lower H_2 column density of $\sim 10^{22} \text{ cm}^{-2}$. They suggest that the clouds are incidentally colliding with each other to trigger the formation of the ~ 20 O-star candidates, which are located within ~ 0.5 pc of the cluster center in the Ring cloud. The collision is evidenced by the bridge feature connecting the two clouds, which is localized toward the O-star candidates. The collision timescale is estimated to be ~ 0.1 Myrs from the cloud size and velocity separation, corresponding the fact that the RCW38 cluster is very young.

In this paper, we report the results of [CI] observations toward RCW38 with ASTE. The wide-field ($6'.0 \times 8'.0 \sim 3 \text{ pc} \times 4 \text{ pc}$) and high-resolution ($17'' \sim 0.14 \text{ pc}$) allowed us to reveal the detailed [CI] gas distributions and physical conditions, such as optical depth and column density. Combining these with the results of past CO observations by Fukui et al. (2016), we investigate the relationship between CO and [CI] emissions around the PDR and molecular clouds in RCW38. Section 2 describes the basic observational setup and data reduction. Section 3 presents the distribution and physical properties of the CO and [CI] emissions. In Section 4, we discuss the relationship between CO and [CI] emissions in RCW38 and investigate the PDR model. We conclude the paper in Section 5.

2 Observation and data reduction

2.1 Observation

We observed RCW38 in the [CI] ($^3P_1 - ^3P_0$; 492.1607 GHz) line with the ASTE 10 m telescope (Ezawa et al. 2004; Kohno et al. 2004) located at Pampa la Bola at an altitude of 4800 m. These observations were remotely conducted on November 26, 2016 from Japan using the remote control system N-COSMOS3 (Kamazaki et al. 2005). We used ALMA Band 8 receiver, which is a dual-polarization side-band separating (2SB) mixer receiver operating at 400–500 GHz (Ito et al. 2018). As a back end, we used the MAC spectrometer, which is a subset of AC45 spectrometer for the Nobeyama 45-m telescope (Sorai et al. 2000). We configured the spectrometer with the mode of 1024-channel power spectrum of 512 MHz bandwidth, which provides a frequency resolution of 0.5 MHz, corresponding to 0.3 km s^{-1} at the [CI] frequency. The telescope half-power beam width (HPBW) is $17''$. We performed on-the-fly (OTF) mapping observations over a $6'.0 \times 8'.0$ area (Sawada et al. 2008), referencing to an off-source position at R.A. = $08^{\text{h}}55^{\text{m}}01^{\text{s}}.51$ and decl. = $-47^{\circ}23'16''.2$ (J2000). The off-source position was free from ^{12}CO line emission in the wide-field CO mapping data by NANTEN2

telescope presented in Fukui et al. (2016). The OTF mapping was performed along each of two orthogonal directions, R.A. and decl. The intervals between the adjacent scans were $6''.0$, which was approximately 1/3 of the HPBW. The data was taken every 0.1 second while the scans were taken at a constant slewing rate of $20'' \text{ sec}^{-1}$, which yielded a spatial sampling interval of $2''.0$. The telescope pointing was checked every two hours by five-point scans of pointing sources: O-Cet [R.A. = $02^{\text{h}}19^{\text{m}}20^{\text{s}}.79$, decl. = $-02^{\circ}58'41''.91$ (J2000)] and IRC+10216 [R.A. = $09^{\text{h}}47^{\text{m}}57^{\text{s}}.41$, decl. = $+13^{\circ}16'43''.60$ (J2000)], and the pointing accuracy was better than $\sim 2''$. The standard chopper-wheel method was used to convert the output signals into antenna temperatures (T_{A}^*), corrected for the atmospheric attenuation. The typical system noise temperature was 800–1400 K in the target directions. These observations were performed as a part of the ASTE demo science project.

2.2 Data reduction

The data were processed using the Common Astronomy Software Applications (CASA version 5.1.1: McMullin et al. 2007). After subtracting the linear baselines from the OTF spectra in the frequency domain, they were convolved with a GJINC (Gaussian \times Jinc) function (Mangum et al. 2007), resampled onto a $6''$ grid, and summed over each 0.6 km s^{-1} velocity bin, resulting in an effective spatial resolution of $\sim 20''$ in HPBW. The adopted main beam efficiency to convert T_{A}^* to main-beam temperature (T_{MB}) is 0.45. Our target line presents bright and spatially extended structures over the observed region, which may additionally contribute to the efficiency due to the error beam of ASTE. Such contribution was estimated to be $< 20\%$ based on the past measurement on Jupiter (private communication). The systematic error of the [CI] amplitude was expected to be 7% in terms of T_{A}^* , which was dominated by the variations of the atmospheric conditions during the observations. Finally, to remove the striping pattern generated along the scan directions, we combined the two maps generated by scanning the R.A. and decl. directions using the basket-weaving method (Emerson & Graeve 1988). The typical rms-noise level in the final cube data is 0.7 K in T_{MB} (corresponding to 0.3 K in T_{A}^*) with a velocity resolution of 0.6 km s^{-1} . The raw data, final cube data, and our detailed analysis procedures are available from the ASTE web page¹.

¹ <https://sites.google.com/site/asteobservation/home/reduction#TOC-DEMO-SCIENCE-DATA-REDUCTION-GUIDE>

2.3 Previous observations

In addition to our [CI] observation, we used the CO data from the previous observations presented in Fukui et al. (2016): $^{12}\text{CO}(1-0)$, $^{13}\text{CO}(1-0)$, and $\text{C}^{18}\text{O}(1-0)$ observations with the 22m ATNF (Australia Telescope National Facility) Mopra millimeter telescope in Australia and $^{12}\text{CO}(3-2)$ observations with the ASTE. The angular resolution and velocity resolution of the Mopra observations were $33''$ and 0.088 km s^{-1} , respectively, and those of the ASTE observations were $22''$ and 0.11 km s^{-1} , respectively. The Mopra and ASTE data were smoothed to an HPBW of $40''$ with a 2D Gaussian function and to 0.6 km s^{-1} velocity resolution (Fukui et al. 2016). The typical rms-noise levels in $^{12}\text{CO}(1-0)$, $^{12}\text{CO}(3-2)$, $^{13}\text{CO}(1-0)$, and $\text{C}^{18}\text{O}(1-0)$ data are 0.4 K, 0.2K, 0.2 K, and 0.1 K, respectively, in T_{MB} with a velocity resolution of 0.6 km s^{-1} . To compare the [CI] data with the CO data and improve signal-to-noise ratios, the ASTE [CI] data were smoothed to an HPBW of $40''$ with a 2D Gaussian function. The typical rms-noise level of the smoothed ASTE [CI] data is 0.3 K in T_{MB} with a velocity resolution of 0.6 km s^{-1} .

3 Results

3.1 [CI] distribution of RCW38

The right panel in Figure 1 shows the [CI] integrated intensity distribution, and YSO and O-star candidates (Wolk et al. 2006; Winston et al. 2011) in RCW38. The [CI] emission has a ring-like structure with a diameter of 1–2 pc. The O-star candidates, including IRS 2, are concentrated in the cavity. Several filamentary and bubble-like structures extend radially outside the ring-like structure by 1–2 pc. These structures are similar to the distribution of $^{13}\text{CO}(1-0)$ and $^{12}\text{CO}(1-0)$ emissions of RCW38 (Fukui et al. 2016). Figure 2 shows the integrated intensity distribution (left and middle) and the declination-velocity diagram (right) of [CI] and $^{13}\text{CO}(1-0)$ emission. The [CI] cloud is composed of two velocity components: Ring cloud ($v_{\text{LSR}} = -8.3\text{--}9.1 \text{ km s}^{-1}$) and Finger cloud ($v_{\text{LSR}} = 9.1\text{--}17.5 \text{ km s}^{-1}$), which are generally similar to those of the CO clouds. The distribution of $^{12}\text{CO}(1-0)$ emission shows intermediate bridge structures between the Ring and Finger clouds (top panel of Figure 3 in Fukui et al. (2016)), whereas the distribution of $^{13}\text{CO}(1-0)$ and [CI] emissions does not trace such structures. Therefore, the distribution of [CI] emission seems to be more similar to that of $^{13}\text{CO}(1-0)$ emission than to that of $^{12}\text{CO}(1-0)$ emission. There are six peaks of [CI] and CO emissions in RCW38: four peaks in the Ring cloud and two peaks in the Finger cloud, whereas the peak positions of [CI] emission are slightly different (\sim

$10''\text{--}30''$) from those of $^{13}\text{CO}(1-0)$ emission. The velocity channel map of the [CI] emission of RCW38 is shown in Appendix 1 (Figure 15).

3.2 Spectrum of [CI] peaks

The top panels in Figure 3 show the spectra of [CI], $^{12}\text{CO}(1-0)$, $^{13}\text{CO}(1-0)$, and $\text{C}^{18}\text{O}(1-0)$ emissions in the six [CI] peaks presented in Figure 2. In all the [CI] peaks of the Ring cloud, there are two or three peaks of $^{12}\text{CO}(1-0)$ emission, which are caused by strong self-absorption (Fukui et al. 2016). In all peaks, the overall velocity structure of [CI] emission is similar to that of $^{13}\text{CO}(1-0)$ emission. The [CI] and $^{13}\text{CO}(1-0)$ emissions in the Ring cloud are also slightly affected by self-absorption. In and around the Finger cloud, we did not detect $\text{C}^{18}\text{O}(1-0)$ emission in any peak. Table 1 shows the peak intensities and integrated intensities of the [CI] and CO emissions towards the peaks.

The bottom panels in Figure 3 show the ratio of [CI]/ $^{13}\text{CO}(1-0)$ intensities ($I_{\text{[CI]}}/I_{^{13}\text{CO}}$) of all peaks. In the Ring cloud, the ratio around the velocity edge ($v_{\text{LSR}} \sim -4\text{--}2$ and/or $7\text{--}9 \text{ km s}^{-1}$) is higher than that around the velocity center, except for the self-absorption velocity range (white circles in Figure 3). In the Finger cloud, the ratio around the large velocity ($v_{\text{LSR}} \sim 13\text{--}15 \text{ km s}^{-1}$) is higher than that around the small velocity ($v_{\text{LSR}} \sim 11\text{--}13 \text{ km s}^{-1}$).

3.3 Intensity ratio of [CI] to $^{13}\text{CO}(1-0)$ emission

Figure 4 shows the distribution of the ratio of [CI]/ $^{13}\text{CO}(1-0)$ integrated intensity (left and middle panels) and the declination-velocity diagram (right panel). The ratio ($W_{\text{[CI]}}/W_{^{13}\text{CO}}$) of the Ring and Finger clouds is 0.5–2.5 and 0.5–4.0, respectively. As seen in the spectra (Figure 3), the ratio around the large velocity ($v_{\text{LSR}} \sim 13\text{--}15 \text{ km s}^{-1}$) of the Finger cloud is higher than that around the small velocity ($v_{\text{LSR}} \sim 11\text{--}13 \text{ km s}^{-1}$). For the Ring cloud, the ratio around the velocity edge ($v_{\text{LSR}} \sim -4\text{--}2$ and/or $7\text{--}9 \text{ km s}^{-1}$) in the middle part of the declination (decl. $\sim -47^\circ 33'00''\text{--}47^\circ 28'00''$) is higher than that around the velocity center. The ratio in the large and small parts of the declination (decl. $\geq -47^\circ 28'00''$ and $\leq -47^\circ 33'00''$) of the Ring cloud is lower than that of the other region. The velocity channel map of the intensity ratio of [CI]/ $^{13}\text{CO}(1-0)$ of RCW38 is shown in Appendix 1 (Figure 16).

Shimajiri et al. (2013) derived point-by-point correlations between the [CI] map and the other line maps ($^{12}\text{CO}(1-0)$, $^{13}\text{CO}(1-0)$, $\text{C}^{18}\text{O}(1-0)$, and H^{13}CO^+) in the OMC-1 region in Orion-A cloud. Consequently, they found

that the [CI] emission has the highest correlation with the $^{13}\text{CO}(1-0)$ emission. Therefore, we also investigate the point-by-point correlations between the [CI] and $^{13}\text{CO}(1-0)$ emissions to compare the result of RCW38 with that of the OMC-1 region (Figure 5). We find that the Ring and Finger clouds also have linear correlations between [CI] and $^{13}\text{CO}(1-0)$ emissions, consistent with the result of the OMC-1 region. From the least-squares fitting, the correlation of the Ring cloud, $I_{13\text{CO}} = 0.64 (\pm 0.00066) I_{[\text{CI}]}$, is found to be very similar to that of the OMC-1 region presented in Shimajiri et al. (2013): $I_{13\text{CO}} = 0.62 I_{[\text{CI}]}$. On the other hand, the Finger cloud has a higher [CI]/ $^{13}\text{CO}(1-0)$ intensity ratio of $I_{13\text{CO}} = 0.47 (\pm 0.0043) I_{[\text{CI}]}$ than the Ring cloud and OMC-1 regions.

3.4 Properties of RCW38

In this section, we derive the physical properties of the molecular clouds in RCW38 (excitation temperature, optical depth, and column density) under the assumption of local thermodynamic equilibrium (LTE).

3.4.1 Excitation temperature (T_{ex})

We assumed that the excitation temperatures (T_{ex}) of [CI] and $^{13}\text{CO}(1-0)$ are identical to that of $^{12}\text{CO}(1-0)$. Since the critical densities of the [CI] ($^3P_1-^3P_0$) and CO(1-0) lines are comparable ($n_{\text{cr}} \sim 10^3 \text{ cm}^{-3}$), similar excitation conditions are expected for those lines (e.g. Ikeda et al. 2002). This is also supported by the similar spatial and velocity structures of the [CI], ^{13}CO , and ^{12}CO emissions (see Section 3.1). The T_{ex} of [CI] and CO transitions is derived from the peak intensity of the $^{12}\text{CO}(1-0)$ emission using the following equation:

$$T_{\text{ex}} = \frac{h\nu/k}{\ln\{1 + (h\nu/k)/(T(^{12}\text{CO}) + J_\nu(T_{\text{BB}}))\}}, \quad (1)$$

where T_{BB} is the temperature of the cosmic background radiation (2.7 K) and J_ν is the radiation temperature, which is given by,

$$J_\nu(T) = \frac{h\nu/k}{\exp(h\nu/kT) - 1}. \quad (2)$$

Using Eq. (2), Eq. (1) is written as follows:

$$T_{\text{ex}} = \frac{5.53}{\ln\{1 + 5.53/(T(^{12}\text{CO}) + 0.819)\}}. \quad (3)$$

Figure 6 shows T_{ex} distribution for the Ring cloud (left panel) and the Finger cloud (right panel). In the Ring cloud, T_{ex} around [CI] peaks rises up to ~ 50 K. In the Finger cloud, T_{ex} around [CI] peaks is lower (~ 25 K) than that in the Ring cloud. However, $^{12}\text{CO}(1-0)$ intensity of the Ring cloud is reduced by the strong self-absorption in the whole region of our [CI] mapping area (e.g., Figure

3), and therefore we might underestimate the T_{ex} of the whole region of the Ring cloud. Fukui et al. (2016) investigated the kinetic temperature (T_{k}) of RCW38 using large velocity gradient (LVG) analysis (e.g., Goldreich, & Kwan 1974) with $^{12}\text{CO}(1-0)$, $^{12}\text{CO}(3-2)$, and $^{13}\text{CO}(1-0)$, and found that the T_{k} in the outskirts of the Ring cloud is higher than 30–50 K (Figure 9 in Fukui et al. 2016). Therefore, we adopt a uniform T_{ex} of 49 K for the Ring cloud in the same manner as in Fukui et al. (2016). For the Finger cloud, we adopt a uniform T_{ex} of 25 K, because the result of the LVG analysis from Fukui et al. (2016) shows that T_{k} of the peak and edge regions of the Finger cloud is higher than 20–30 K (Figure 10 in Fukui et al. (2016)) and the $^{12}\text{CO}(1-0)$ emission at the edges of the Finger clouds is not optically thick because this region is more diffuse than the other regions of the cloud. We examine the possible uncertainties caused by these assumptions in section 4.2. In addition, we present the results by employing a non-uniform distribution of T_{ex} (see Figure 6) in Appendix 2.

3.4.2 Optical depth and column density

Under the assumption of LTE, the total beam-averaged column density of [CI], $N([\text{CI}])$, is given as follows:

$$N([\text{CI}]) = \frac{8\pi k\nu^2}{3c^3 h A_{10}} \times \int T_{\text{MB}} \frac{\tau_{[\text{CI}]}}{1 - e^{-\tau_{[\text{CI}]}}} dv \times Q(T_{\text{ex}}) \exp\left(\frac{E_1}{kT_{\text{ex}}}\right) \left[1 - \frac{J_\nu(T_{\text{BB}})}{J_\nu(T_{\text{ex}})}\right]^{-1}, \quad (4)$$

where $Q(T_{\text{ex}})$ is the ground-state partition function for the carbon atom, A_{10} is the Einstein A coefficient for the $^3P_1-^3P_0$ transition, and τ is the optical depth. The factor $(8\pi k\nu^2)/(3c^3 h A_{10})$ is calculated to be $1.98 \times 10^{15} \text{ cm}^{-2} (\text{K km s}^{-1})^{-1}$. The partition function is described as

$$Q(T_{\text{ex}}) = 1 + 3 \exp\left(-\frac{E_1}{kT_{\text{ex}}}\right) + 5 \exp\left(-\frac{E_2}{kT_{\text{ex}}}\right), \quad (5)$$

where E_1 and E_2 represent the energies of the $J = 1$ level ($E_1/k = 23.6$ K) and the $J = 2$ level ($E_2/k = 62.5$ K). The optical depth of [CI], $\tau_{[\text{CI}]}$, is given by

$$\tau = -\ln\left\{1 - \frac{T_{\text{MB}}}{J_\nu(T_{\text{ex}}) - J_\nu(T_{\text{BB}})}\right\}. \quad (6)$$

Using Eqs. (2), (5), and (6), Eq. (4) is written as follows:

$$N([\text{CI}]) = 4.67 \times 10^{16} \frac{1 + 3e^{-23.6/T_{\text{ex}}} + 5e^{-62.5/T_{\text{ex}}}}{1 - e^{-23.6/T_{\text{ex}}}} \int \tau_{[\text{CI}]} dv. \quad (7)$$

On the other hand, the column density of CO, $N(\text{CO})$, is estimated using the optical depth of $^{13}\text{CO}(1-0)$, $\tau_{13\text{CO}}$, and the integrated intensity of the $^{13}\text{CO}(1-0)$ emission:

$$N(\text{CO}) = [^{12}\text{CO}]/[^{13}\text{CO}] \times 4.57 \times 10^{13} \int T_{\text{MB}} \frac{\tau_{13\text{CO}}}{1 - e^{-\tau_{13\text{CO}}}} dv$$

$$\begin{aligned}
& \times \left(T_{\text{ex}} + \frac{hB}{3k} \right) \exp \left(\frac{h\nu}{kT_{\text{ex}}} \right) \left[1 - \frac{J_\nu(T_{\text{BB}})}{J_\nu(T_{\text{ex}})} \right]^{-1} \\
& = [^{12}\text{CO}]/[^{13}\text{CO}] \times 2.42 \\
& \times 10^{14} \frac{T_{\text{ex}} + 0.87}{1 - e^{-5.29/T_{\text{ex}}}} \int \tau_{^{13}\text{CO}} dv, \quad (8)
\end{aligned}$$

where B is the rigid rotor rotation constant, the abundance ratio of $^{12}\text{CO}/^{13}\text{CO}$ ($[^{12}\text{CO}]/[^{13}\text{CO}]$) is assumed to be 77 (Wilson & Rood 1994), and $\tau_{^{13}\text{CO}}$ is estimated by Eq. (6). Eqs. (1)–(7) were quoted from Oka et al. (2001) and Ikeda et al. (2002). Eq. (8) was quoted from Mangum, & Shirley (2015).

Figure 7 shows the optical depth of the [CI] ($\tau_{\text{[CI]}}$) and ^{13}CO ($\tau_{^{13}\text{CO}}$) distributions of the six [CI] peaks. Further, $\tau_{\text{[CI]}}$ and $\tau_{^{13}\text{CO}}$ are 0.1–0.6 and 0.1–0.3, respectively, suggesting optically thin emission. However, we note that self-absorption structures are present in the [CI] and ^{13}CO spectra around the [CI] peaks (Figure 3) therefore, [CI] and ^{13}CO around strong peaks might be moderately optically thick. Therefore, the [CI] and CO column densities in the Ring cloud are considered to be slightly underestimated. We examined the possible underestimation caused by the self-absorption in section 4.2. Table 2 summarizes the properties (such as temperature, optical depth, and column density) of the six [CI] peaks in the Ring and Finger clouds. We estimated the error of column densities by varying the assumed T_{ex} of the Ring and Finger clouds from 30 K to 80 K and from 20 K to 30 K, respectively. The details of the fluctuations are discussed in Section 4.2.

Figure 8 shows the [CI] (Top) and H_2 (Bottom) column density distributions of RCW38. The H_2 column density is estimated under the assumption of the abundance ratio of $\text{H}_2/^{12}\text{CO} = 10^4$ (e.g., Frerking et al. 1982; Leung et al. 1984). As a result, we estimated the [CI] column density of the Ring and Finger clouds to be $(0.1\text{--}1.4) \times 10^{18}$ and $(0.1\text{--}0.2) \times 10^{18} \text{ cm}^{-2}$, respectively, and the H_2 column density of the Ring and Finger clouds to be $(0.1\text{--}1.2) \times 10^{23}$ and $\sim 0.1 \times 10^{23} \text{ cm}^{-2}$, respectively. Figure 9 shows the ratio of [CI]/CO column density ($N_{\text{[CI]}}/N_{\text{CO}}$) distribution of RCW38. The ratio in the Ring and Finger clouds are 0.05–0.15 and 0.1–0.5, respectively.

3.4.3 [CI] - H_2 conversion factor

Figure 10 shows the relationship between the [CI] integrated intensity ($W_{\text{[CI]}}$) and H_2 column density (N_{H_2}) derived from the $^{13}\text{CO}(1\text{-}0)$ emission. We also calculated A_V using the relationship between the H_2 column density and the visual extinction: $N_{\text{H}_2}/A_V = 9.4 \times 10^{20} \text{ cm}^{-2} \text{ mag}^{-1}$ (Frerking et al. 1982) and put A_V into Figure 10. Both the Ring and Finger clouds have a linear relationship between $W_{\text{[CI]}}$ and N_{H_2} . To estimate the conversion

factor from $W_{\text{[CI]}}$ to N_{H_2} ($X_{\text{[CI]}} = N_{\text{H}_2}/W_{\text{[CI]}}$), we used the least-squares fitting method for the Ring cloud ($N_{\text{H}_2} \gtrsim 10^{22} \text{ cm}^{-2}$; $A_V \gtrsim 10 \text{ mag}$) and the Finger cloud ($N_{\text{H}_2} \lesssim 10^{22} \text{ cm}^{-2}$; $A_V \lesssim 10 \text{ mag}$). The conversion factors of the Ring and Finger clouds are $X_{\text{[CI]}} = 1.4 (\pm 0.004) \times 10^{21} \text{ cm}^{-2} \text{ K}^{-1} \text{ km}^{-1} \text{ s}$ (corresponding to $W_{\text{[CI]}} = 7.4 (\pm 0.02) \times 10^{-22} N_{\text{H}_2}$) and $X_{\text{[CI]}} = 6.3 (\pm 0.08) \times 10^{20} \text{ cm}^{-2} \text{ K}^{-1} \text{ km}^{-1} \text{ s}$ (corresponding to $W_{\text{[CI]}} = 1.6 (\pm 0.02) \times 10^{-21} N_{\text{H}_2}$), respectively.

Offner et al. (2014) calculated $X_{\text{[CI]}}$ for typical molecular clouds with low-UV ($G_0 = 1$ and 10) in the Milky Way using numerical simulations. They demonstrated that [CI] is a good tracer of molecular gas distribution for column densities of up to $6 \times 10^{23} \text{ cm}^{-2}$ (corresponding to $A_V \sim 600$), and derived the average $X_{\text{[CI]}}$ of $1.1 \times 10^{21} \text{ cm}^{-2} \text{ K}^{-1} \text{ km}^{-1} \text{ s}$ (corresponding to $W_{\text{[CI]}} = 9.1 \times 10^{-22} N_{\text{H}_2}$). They also reported that $X_{\text{[CI]}}$ increases strongly with N_{H_2} : from $X_{\text{[CI]}} \sim 10^{21} \text{ cm}^{-2} \text{ K}^{-1} \text{ km}^{-1} \text{ s}$ at $N_{\text{H}_2} = 10^{21} \text{ cm}^{-2}$ to $X_{\text{[CI]}} \sim 10^{22} \text{ cm}^{-2} \text{ K}^{-1} \text{ km}^{-1} \text{ s}$ at $N_{\text{H}_2} = 10^{23} \text{ cm}^{-2}$ (see Figure 3 in Offner et al. 2014 for $G_0 = 10$), which is consistent with our results (that $X_{\text{[CI]}}$ of the Ring cloud is larger than that of the Finger cloud). We note that the UV intensities used for the simulation are significantly smaller than those in the massive star-forming regions, such as the Orion and the Carina nebulae ($G_0 \sim 10^4\text{--}10^5$) similar to RCW38. However, the intensity is considered to be attenuated inside molecular cloud, and the intensities inside the RCW38 clouds are therefore similar to those used in the simulation.

4 Discussion

4.1 Relation between [CI] and $^{13}\text{CO}(1\text{-}0)$ emission

From our [CI] observations and previous CO observations (Fukui et al. 2016) for RCW38, we find that the spatial and velocity distributions of the [CI] emission are very similar to those of the $^{13}\text{CO}(1\text{-}0)$ emission in RCW38 (Figures 2 and 3). These results are consistent with those from past [CI] observations (e.g., Ikeda et al. 2002; Shimajiri et al. 2013). In particular, the ratio of [CI]/ $^{13}\text{CO}(1\text{-}0)$ intensity ($I_{\text{[CI]}}/I_{^{13}\text{CO}}$) of the Ring cloud is the same as that of the OMC-1 region in the Orion A cloud (Shimajiri et al. 2013). These ratios are lower than that of the Finger cloud (Figure 5). The integrated intensity ratio ($W_{\text{[CI]}}/W_{^{13}\text{CO}}$) of the Ring cloud is also lower than that of the Finger cloud (Figure 4). This trend may be related to the lower H_2 column density of the Finger cloud ($N_{\text{H}_2} \sim 10^{21}\text{--}10^{22} \text{ cm}^{-2}$), which is smaller than that of the Ring cloud and the Orion A cloud ($N_{\text{H}_2} \sim 10^{22}\text{--}10^{23} \text{ cm}^{-2}$) by about an order of magnitude. The Finger cloud may be affected

more by UV radiation due to the small H_2 column density. However, we note that a small H_2 column density does not always produce a high-ratio of $W_{[CI]}/W_{13CO}$. Figure 4 shows the low-ratio of $W_{[CI]}/W_{13CO}$ (~ 0.5 – 1.5) in the outer region of the Ring cloud, which has lower H_2 column density ($N_{H_2} \sim 10^{22} \text{ cm}^{-2}$ in the bottom panel of Figure 8) than in the inside region (ratio: ~ 1.5 – 2.5) of the Ring cloud ($N_{H_2} \sim 10^{23} \text{ cm}^{-2}$ in the bottom panel of Figure 8). It might be caused by the lower density of UV photons in the outer region because this region is far from the central O-star (IRS 2) and is more strongly shielded than the dense molecular gas inside the Ring cloud. This is consistent with a lower $^{12}\text{CO}(3-2)/^{12}\text{CO}(1-0)$ intensity ratio (~ 0.3), suggesting a lower temperature in the outer region of the Ring cloud than in the inside region (ratio of ~ 0.5 – 1.5 in Figure 11; Fukui et al. 2016).

4.2 Relation between ratio of [CI]/[CO] abundance and H_2 column density

The top panel of Figure 12 shows the relationship between the ratios of [CI]/ $^{13}\text{CO}(1-0)$ integrated intensity ($W_{[CI]}/W_{13CO}$) and H_2 column density (N_{H_2}), and the bottom panel shows the relationship between the ratio of [CI]/CO column density ($N_{[CI]}/N_{CO}$) and N_{H_2} . We also show A_V , which is calculated from N_{H_2} (Frerking et al. 1982) in Figure 12. In the low- A_V region ($A_V \leq 10$ mag), $W_{[CI]}/W_{13CO}$ decreases with A_V from ~ 5 to ~ 1 . In the high- A_V region ($A_V > 10$ mag), $W_{[CI]}/W_{13CO}$ is nearly constant (~ 1.5) for A_V of up to 100 mag. A similar trend is seen in the relationship between $N_{[CI]}/N_{CO}$ and A_V (N_{H_2}). In the low- A_V region ($A_V \leq 10$ mag), $N_{[CI]}/N_{CO}$ decreases with A_V from ~ 0.6 to ~ 0.2 . In the high- A_V region ($A_V > 10$ mag), $N_{[CI]}/N_{CO}$ is constant (~ 0.1) for A_V of up to 100 mag. Table 3 summarizes the average and standard deviations of $W_{[CI]}/W_{13CO}$ and $N_{[CI]}/N_{CO}$ for the Ring and Finger clouds. This shows that a large amount of [CI] with $\sim 10\%$ of CO abundance exists even in the high column density region of A_V up to 100 mag. This result is generally consistent with that of Orion A and B clouds by Ikeda et al. (2002), but the method is slightly different from the present method. We recalculated $N_{[CI]}/N_{CO}$ of Orion A and B clouds using a $^{12}\text{CO}/^{13}\text{CO}$ abundance ratio of 77 (Wilson & Rood 1994), instead of 60 adopted by Ikeda et al. (2002). In addition, we set the display range of N_{H_2} for Orion A and B clouds as $10^{21} \leq N_{H_2} \leq 4.0 \times 10^{22} \text{ cm}^{-2}$, which corresponds to a range of about 60% of the whole data points in Figure 13 of Ikeda et al. (2002). The density of the Ring and Finger clouds were estimated to be larger than 10^3 cm^{-3} according to the previous LVG analysis in Fukui et al. (2016). In this case, the

$[^{12}\text{CO}]/[^{13}\text{CO}]$ abundance ratio may present spatial variations only over the relatively narrow clouds edge, which may be caused by selective photo-dissociation (e.g. Warin et al. 1996; Szűcs et al. 2014). Some chemical processes may also alter the $[^{12}\text{CO}]/[^{13}\text{CO}]$ abundance ratio. The simulation of Szűcs et al. (2014) suggested that the chemical fractionation causes a factor of 2–3 decrease at intermediate cloud depth ($10^{15} \text{ cm}^{-2} \lesssim N(^{12}\text{CO}) \lesssim 10^{17} \text{ cm}^{-2}$). If we adopt a more realistic $[^{12}\text{CO}]/[^{13}\text{CO}]$ distribution, the actual $N_{[CI]}/N_{CO}$ values can be slightly higher than our present derivations. Thus, the uniform $[^{12}\text{CO}]/[^{13}\text{CO}]$ is adopted in this paper provides the conservative lower limits of $N_{[CI]}/N_{CO}$.

Figure 13 shows the relationship between $N_{[CI]}/N_{CO}$ and N_{H_2} for the inner, outer, and the other regions of the Ring cloud. We defined the outer region of the Ring cloud by a low-integrated intensity of $^{13}\text{CO}(1-0)$: lower than 10 K km s^{-1} , which corresponds to a value of 20σ (black thick contour in Figure 11). We defined the inner region of the Ring cloud as the central region around IRS 2 (white box in Figure 11). The average ratio of $N_{[CI]}/N_{CO}$ (and standard deviation) in the outer, inner, and other regions is 0.090 (std: 0.086), 0.11 (std: 0.0083), and 0.11 (std: 0.019), respectively. The $N_{[CI]}/N_{CO}$ ratio in the outer region is lower than that in the other and inner regions except for the low-column density ($N_{H_2} \lesssim 10^{22} \text{ cm}^{-2}$), where the ratio becomes higher due to the diffuse distribution of molecular gas. The $N_{[CI]}/N_{CO}$ ratio in the inner region is slightly higher than that in the other region, especially for the high-column density ($N_{H_2} \gtrsim 3 \times 10^{22} \text{ cm}^{-2}$). The variation in the ratios suggest that the outer region is affected less and the inner region is affected more by UV photons than in the other region. This result is consistent with the physical association between the Ring cloud and the cluster in RCW38 reported by Fukui et al. (2016): cluster is located in and ionizes the central cavity of the Ring cloud.

Next, we discuss the effect of uncertainty in T_{ex} on the $N_{[CI]}/N_{CO}$. To assess the biases caused by self-absorption, we re-constructed spectra corrected from the absorption of $^{12}\text{CO}(1-0)$, $^{13}\text{CO}(1-0)$, and [CI] by fitting gaussian profile to them for 6 [CI] peaks (Figure 14). The highest reconstructed $^{12}\text{CO}(1-0)$ intensity corresponds to a T_{ex} of 80 K. On the other hand, the previous LVG analysis derived that the lowest T_{ex} in the Ring cloud is $\sim 30 \text{ K}$ (Fukui et al. 2016). The uncertainties of $N_{[CI]}/N_{CO}$ in the Ring cloud can be gauged by changing the assumed T_{ex} from 30 K to 80 K. Similarly, to be consistent with the previous LVG analysis (Fukui et al. 2016), we changed the assumed T_{ex} from 20 K to 30 K to assess the uncertainty of $N_{[CI]}/N_{CO}$ in the Finger cloud. From Eqs. (6)–(8) in Section 3.4.2, $N_{[CI]}/N_{CO}$ is written as follows:

$$N_{[\text{CI}]} / N_{\text{CO}} = \alpha R(\tau) f(T_{\text{ex}}), \quad (9)$$

$$\alpha = 2.51, \quad (10)$$

$$\begin{aligned} R(\tau) &= \frac{\int \tau_{[\text{CI}]} dv}{\int \tau_{^{13}\text{CO}} dv} \\ &= \frac{\int \ln \left\{ 1 - \frac{T_{\text{MB}}([\text{CI}])}{J_\nu(T_{\text{ex}}) - J_\nu(T_{\text{BB}})} \right\} dv}{\int \ln \left\{ 1 - \frac{T_{\text{MB}}(^{13}\text{CO})}{J_\nu(T_{\text{ex}}) - J_\nu(T_{\text{BB}})} \right\} dv} \\ &= R(T_{\text{MB}}, T_{\text{ex}}), \end{aligned} \quad (11)$$

$$f(T_{\text{ex}}) = \frac{(1 + 3e^{-23.6/T_{\text{ex}}} + 5e^{-62.5/T_{\text{ex}}})(1 - e^{-5.29/T_{\text{ex}}})}{(1 - e^{-23.6/T_{\text{ex}}})(T_{\text{ex}} + 0.87)}. \quad (12)$$

For the Ring cloud, $R(T_{\text{MB}}, T_{\text{ex}})$ and $f(T_{\text{ex}})$ change from $\sim 140\%$ to $\sim 90\%$ of $R(T_{\text{MB}}, 49\text{K})$ and $\sim 130\%$ to $\sim 70\%$ of $f(49\text{K})$, respectively, with T_{ex} changing from 30 K to 80 K. For the Finger cloud, $R(T_{\text{MB}}, T_{\text{ex}})$ and $f(T_{\text{ex}})$ change from $\sim 120\%$ to $\sim 90\%$ of $R(T_{\text{MB}}, 25\text{K})$ and $\sim 110\%$ to $\sim 90\%$ of $f(25\text{K})$, respectively, with T_{ex} changing from 20 K to 30 K. Therefore, the possible value of $N_{[\text{CI}]} / N_{\text{CO}}$ in the Ring cloud is $\sim 0.2\text{--}0.06$ by considering the uncertainty of T_{ex} (see error values in Table 2). The possible value of $N_{[\text{CI}]} / N_{\text{CO}}$ in the Finger cloud is higher than that in the Ring cloud ($\gtrsim 0.2$).

Self-absorption may cause $N_{[\text{CI}]}$ and N_{CO} to be underestimated. For 5 [CI] peaks², the $N_{[\text{CI}]}$ and N_{CO} derived from the directly observed spectra are about 80–95 % and 80–90 % of those derived based on the gaussian-reconstructed [CI] and $^{13}\text{CO}(1-0)$ spectra. These results indicated that the self-absorption of [CI] and $^{13}\text{CO}(1-0)$ have minor effect on $N_{[\text{CI}]}$, N_{CO} , and $N_{[\text{CI}]} / N_{\text{CO}}$.

Our main conclusions from this section are: 1) $N_{[\text{CI}]} / N_{\text{CO}}$ is approximately 0.1 for A_V of up to 100 mag and 2) variation in UV irradiation between each region of the Ring cloud (inner, outer, and the other regions) is detected, and it is not dependent on our T_{ex} assumption (uniform T_{ex} for the Ring and Finger clouds). We present the results in which T_{ex} is derived from the peak intensity of $^{12}\text{CO}(1-0)$ (see Figure 6) in Appendix 2.

4.3 PDR model

The present analysis shows that the [CI]/CO abundance ratio is ~ 0.1 over a wide range of A_V (10–100 mag), whereas it varies from ~ 0.5 to ~ 0.1 for A_V of less than 10 mag. This behavior is generally consistent with that of the PDR model predicted by the classical layered distribution, whereas the large [CI] abundance at large A_V is not consistent with the model (e.g. Röllig et al. 2007). The present results further evident the large residual [CI] in the deep

interiors of a molecular cloud having A_V of a few 10 to 100 mag, which are consistent with the previous observations of the Orion and the other regions (e.g., Ikeda et al. 2002; Shimajiri et al. 2013; Burton et al. 2015). Glover et al. (2015) presented the model calculations of [CI] and CO in a highly turbulent cloud of $A_V \sim 10$ mag, and showed that an inhomogeneous cloud allows the UV radiation to penetrate the cloud deeply at $A_V \sim 10$ mag. This cloud is similar to a low column density cloud, such as Taurus (e.g., Mizuno et al. 1995), whereas RCW38 is a giant molecular cloud (GMC) whose column density is 10 times larger than that of in Taurus. This indicates that carbon ionizing photons of 11–13.6 eV deeply penetrate a GMC. We suggest that such high [CI] abundance generally indicates a highly clumpy density distribution in a GMC. The present resolution of the Mopra and ASTE telescopes, i.e., ~ 0.3 pc, may be insufficient to resolve such clumps. For a better understanding, we plan high-resolution [CI] observations toward RCW38 with ALMA. The expected clumped distribution is in fact directly shown by the recent high-resolution C^{18}O image of RCW38 at 0.02 pc resolution obtained with ALMA (Torii et al. 2019), where dense cores of size 0.02–0.08 pc exhibit clumpy and filamentary distribution. This distribution is compared with the magnetohydrodynamical numerical simulations of colliding molecular flows (Inoue & Fukui 2013). By synthetic observations of the numerical simulations, Fukui et al. (2019) demonstrated that the core mass function and the size distribution indicate that the cores are sufficiently massive to form high mass stars, suggesting that clumped distribution may be an important stage prior to a high mass star formation in a GMC. It remains to be investigated further if the clumpy distribution of the [CI] gas in RCW38 was created because of cloud-cloud collision, while the collision is a process which creates the clumpy distribution. We cautiously include an alternative possibility that the distribution may be a general property of the dense gas in a GMC, independent of the past cloud-collision episode. To clarify this issue, we need to extend [CI] observations to other GMCs having different environments and histories.

5 Summary

We present the results of [CI] observations toward the super star cluster RCW38 with the ASTE 10 m sub-mm telescope. Our main results are as follows.

1. The overall distribution of [CI] emission is similar to that of $^{13}\text{CO}(1-0)$ emission presented in Fukui et al. (2016), including two velocity components: Ring cloud ($v_{\text{LSR}} = -8.3\text{--}9.1$ km s⁻¹) and Finger cloud ($v_{\text{LSR}} = 9.1\text{--}17.5$ km s⁻¹). These results are consistent with

² We could not detect any self-absorption features of [CI] and ^{13}CO emission in one peak (labeled as F) out of the six [CI] peaks

those of the past [CI] observations (e.g., Ikeda et al. 2002; Shimajiri et al. 2013).

2. By assuming that the T_{ex} for the Ring and Finger clouds are 49 K and 25 K, respectively, as derived from the $^{12}\text{CO}(1-0)$ emission, the optical depth of the [CI] emission is found to be τ of 0.1–0.6, suggesting mostly optically thin emission. The column densities of [CI] of the Ring and Finger clouds are $(0.1\text{--}1.4) \times 10^{18}$ and $(0.1\text{--}0.2) \times 10^{18} \text{ cm}^{-2}$, respectively.
3. An empirical conversion factor from the [CI] integrated intensity to the H_2 column density was estimated to be $X_{[\text{CI}]} = 6.3 \times 10^{20} \text{ cm}^{-2} \text{ K}^{-1} \text{ km}^{-1} \text{ s}$ at A_V of less than 10 mag, and $X_{[\text{CI}]} = 1.4 \times 10^{21} \text{ cm}^{-2} \text{ K}^{-1} \text{ km}^{-1} \text{ s}$ for A_V of 10–100 mag.
4. The column density ratio of [CI] to CO ($N_{[\text{CI}]} / N_{\text{CO}}$) was estimated as ~ 0.1 for A_V of 10–100 mag. This value is consistent with that of the Orion A and B clouds (Ikeda et al. 2002). The present results encompass a large A_V (of up to 100 mag) than that for Orion (which covers A_V of up to ~ 60 mag).
5. The results are consistent with the highly clumped density distributions revealed by the recent ALMA observations of C^{18}O by Torii et al. (2019). Numerical simulations of colliding molecular gas flows show that dense cores of similar sizes are formed via compression, which further corroborates the clumped distribution suggested by the high [CI] abundance in the deep interiors of GMC with A_V of ~ 100 mag.

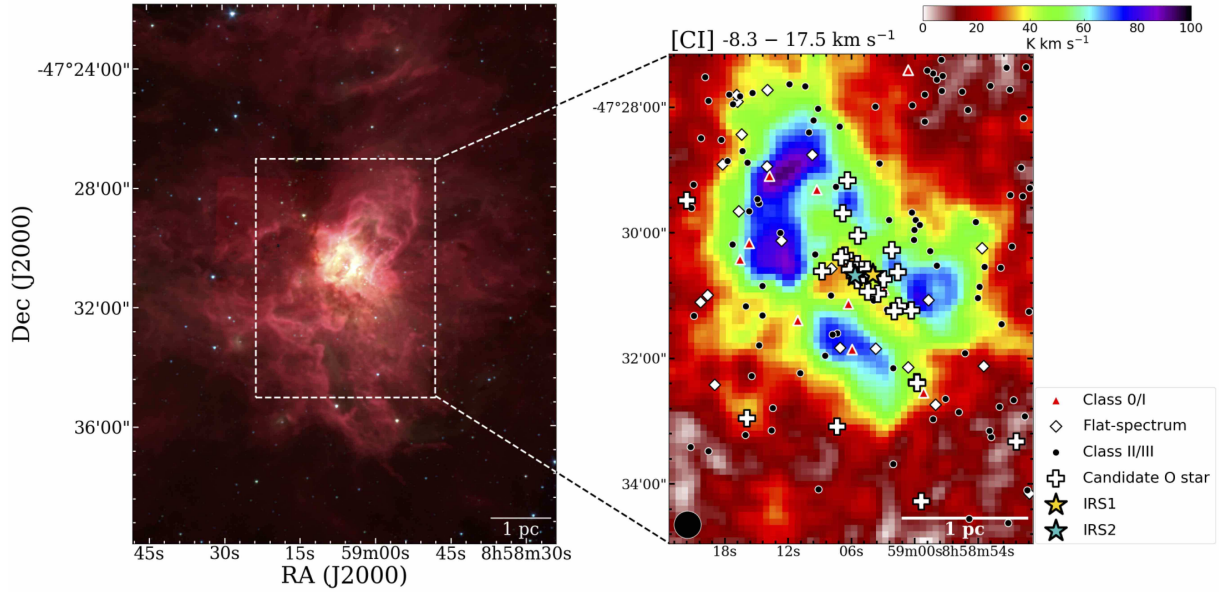


Fig. 1. Mid-infrared pseudo color image of RCW38 (Left: Winston et al. 2011) and [CI] integrated intensity distributions of RCW38 (Right). The color image was produced by combining the 3.6, 4.5, and 8.6 μm images from *Spitzer* data. The white dashed box in the left panel shows the mapping size of the ASTE observation ($6' \times 8'$). YSOs and O star candidates obtained by Wolk et al. (2006) and Winston et al. (2011) are plotted in the right panel. Red triangles and white diamonds indicate the class 0/I and flat-spectrum YSOs, respectively. Black circles indicate the class II and class III YSOs (Winston et al. 2011). White crosses indicate the O-star candidates. Yellow and cyan star symbols indicate the peaks of IRS 1 and IRS 2, respectively (Wolk et al. 2006). These data were smoothed to an HPBW of $26''$ with a 2D Gaussian function, and the rms noise level was reduced to a typical value of 0.5 K in T_{MB} . The black filled circle at the lower left corner in the right panel shows the HPBW size.

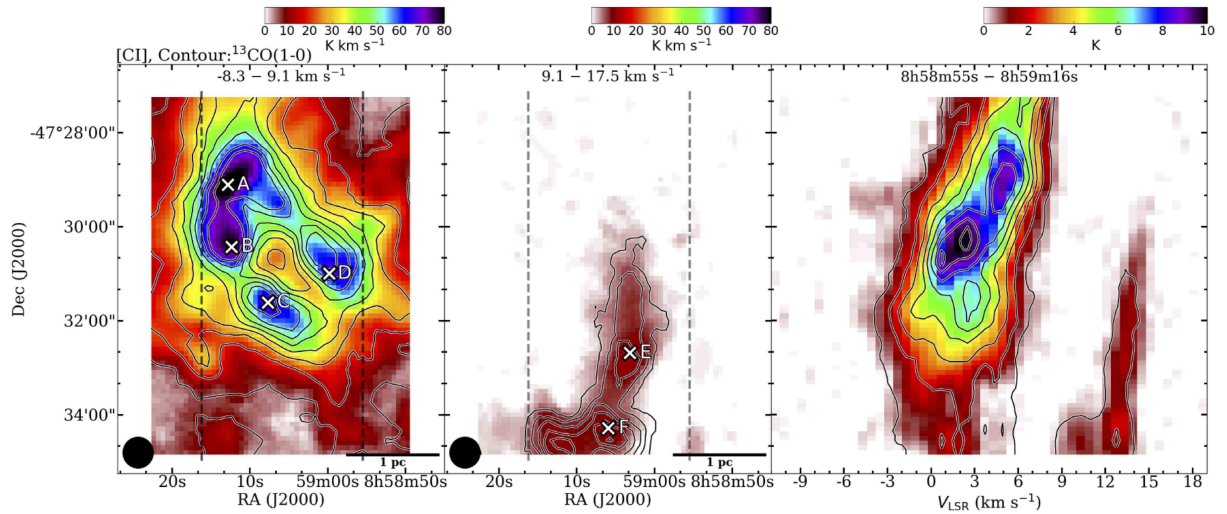


Fig. 2. [CI] integrated intensity distributions of RCW 38 (Left: Ring cloud, Middle: Finger cloud) and declination-velocity diagram (Right). The black contours show the integrated intensity distribution and declination-velocity diagram of the $^{13}\text{CO}(1-0)$ emission. Contour levels of the Ring cloud are 3σ , 13σ , 23σ , 33σ , 43σ , 53σ , 63σ , 73σ , and 83σ ($1\sigma = 0.5 \text{ K km s}^{-1}$). Contour levels of the Finger cloud are 3σ , 5σ , 7σ , 9σ , 11σ , 13σ , 15σ , and 17σ ($1\sigma = 0.4 \text{ K km s}^{-1}$). Contour levels of the declination-velocity diagram are 3σ , 13σ , 23σ , 33σ , 43σ , 53σ , 63σ , and 73σ ($1\sigma = 0.09 \text{ K}$). The vertical dashed lines indicate the integration range in the declination-velocity diagram. The ASTE [CI] data were smoothed to an HPBW of $40''$ with a 2D Gaussian function for comparison with the Mopra $^{13}\text{CO}(1-0)$ data. The black filled circles at the lower left corners show the HPBW of the [CI] and the CO data ($40''$). The six white cross symbols (designated from A to F) indicate the position of the [CI] peaks.

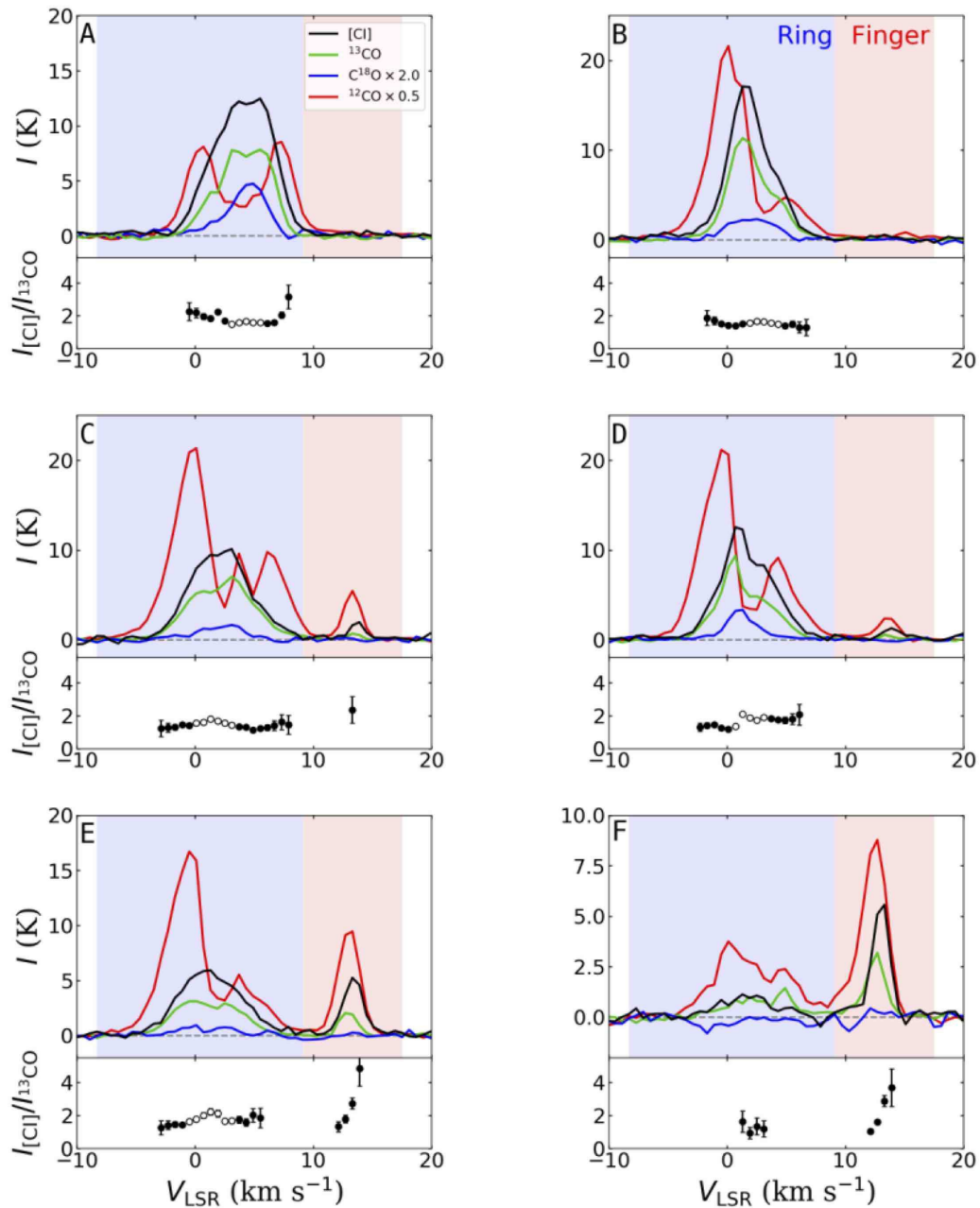


Fig. 3. Averaged spectra of the [Cl] and CO emissions for the six [Cl] peaks detected. The spectra were obtained by averaging the intensities in a circle centered at the peak positions and with a radius of $20''$, corresponding to the HPBW of the [Cl] and CO data. [Cl], $^{13}\text{CO}(1-0)$, $\text{C}^{18}\text{O}(1-0)$, and $^{12}\text{CO}(1-0)$ are indicated by black, green, blue, and red lines, respectively. Intensities of the $\text{C}^{18}\text{O}(1-0)$ and $^{12}\text{CO}(1-0)$ are multiplied by 2.0 and 0.5, respectively. The blue and red areas indicate the velocity range of the Ring cloud (-8.3 – 9.1 km s^{-1}) and the Finger cloud (9.1 – 17.5 km s^{-1}), respectively. The ratio of the [Cl]/ ^{13}CO intensities ($I_{[\text{Cl}]} / I_{^{13}\text{CO}}$) for the six [Cl] peaks is presented at the bottom of each spectrum. These ratios are only derived in v_{LSR} with $I_{[\text{Cl}]} \geq 3\sigma_{[\text{Cl}]}$ and $I_{^{13}\text{CO}} \geq 3\sigma_{^{13}\text{CO}}$ ($1\sigma_{[\text{Cl}]} = 0.2$ K, $1\sigma_{^{13}\text{CO}} = 0.1$ K). The black and white circles indicate the ratios that are affected and not affected by self-absorption, respectively. Error bars represent 1σ value of the ratio.

Table 1. [C] and CO peak intensities and integrated intensities of 6 [C] peaks

Name	R.A.(J2000)	Decl.(J2000)	Line	T_{peak} (K)		$\int T_{\text{MB}} dv$ (K km s $^{-1}$)	
				Ring	Finger	Ring	Finger
A	8:59:12.86	-47:29:06.52	[C]	12.5 \pm 0.3	—*	78.0 \pm 3.0	—
			$^{13}\text{CO}(1-0)$	7.8 \pm 0.2	—	44.0 \pm 2.0	—
			$\text{C}^{18}\text{O}(1-0)$	2.4 \pm 0.1	—	9.1 \pm 1.0	—
			$^{12}\text{CO}(1-0)$	17.1 \pm 0.4	4.1 \pm 0.4	110.0 \pm 5.0	3.7 \pm 0.5
B	8:59:12.35	-47:30:25.55	[C]	17.1 \pm 0.3	—	73.0 \pm 3.0	—
			$^{13}\text{CO}(1-0)$	11.3 \pm 0.2	—	47.0 \pm 2.0	—
			$\text{C}^{18}\text{O}(1-0)$	1.2 \pm 0.1	—	5.4 \pm 0.6	—
			$^{12}\text{CO}(1-0)$	43.2 \pm 0.4	1.7 \pm 0.4	190.0 \pm 6.0	1.8 \pm 0.5
C	8:59:07.70	-47:31:36.79	[C]	10.1 \pm 0.3	2.0 \pm 0.3	62.0 \pm 3.0	2.1 \pm 0.4
			$^{13}\text{CO}(1-0)$	7.0 \pm 0.2	0.7 \pm 0.2	43.0 \pm 2.0	0.4 \pm 0.1
			$\text{C}^{18}\text{O}(1-0)$	0.8 \pm 0.1	—	3.0 \pm 0.5	—
			$^{12}\text{CO}(1-0)$	42.7 \pm 0.4	10.9 \pm 0.4	240.0 \pm 6.0	22.0 \pm 2.0
D	8:58:59.84	-47:30:59.76	[C]	12.6 \pm 0.3	1.3 \pm 0.3	59.0 \pm 3.0	1.9 \pm 0.5
			$^{13}\text{CO}(1-0)$	9.4 \pm 0.2	—	38.0 \pm 2.0	—
			$\text{C}^{18}\text{O}(1-0)$	1.7 \pm 0.1	—	4.4 \pm 0.4	—
			$^{12}\text{CO}(1-0)$	42.3 \pm 0.4	4.8 \pm 0.4	200.0 \pm 6.0	9.9 \pm 1.0
E	8:59:03.18	-47:32:41.20	[C]	6.0 \pm 0.3	5.2 \pm 0.3	37.0 \pm 3.0	10.0 \pm 0.9
			$^{13}\text{CO}(1-0)$	3.1 \pm 0.2	2.0 \pm 0.2	20.0 \pm 2.0	3.7 \pm 0.5
			$\text{C}^{18}\text{O}(1-0)$	0.5 \pm 0.1	—	1.3 \pm 0.5	—
			$^{12}\text{CO}(1-0)$	33.4 \pm 0.4	18.9 \pm 0.4	160.0 \pm 6.0	45.0 \pm 2.0
F	8:59:05.97	-47:34:17.29	[C]	1.1 \pm 0.3	5.6 \pm 0.3	2.5 \pm 0.7	9.5 \pm 0.7
			$^{13}\text{CO}(1-0)$	1.4 \pm 0.2	3.2 \pm 0.2	4.5 \pm 1.0	6.1 \pm 0.7
			$\text{C}^{18}\text{O}(1-0)$	—	—	—	—
			$^{12}\text{CO}(1-0)$	7.5 \pm 0.4	17.6 \pm 0.4	46.0 \pm 5.0	49.0 \pm 2.0

* T_{peak} is less than 3σ ($1\sigma_{[\text{C}]} = 0.3$ K, $1\sigma_{^{13}\text{CO}(1-0)} = 0.2$ K, $1\sigma_{\text{C}^{18}\text{O}(1-0)} = 0.1$ K, $1\sigma_{^{12}\text{CO}(1-0)} = 0.4$ K)

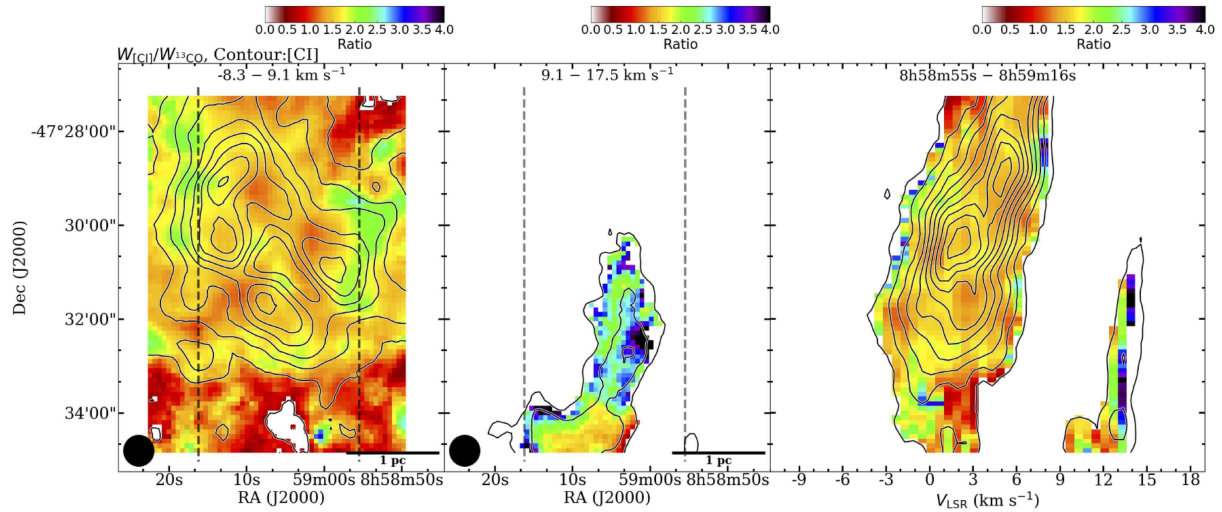


Fig. 4. Ratio of the [CI] / $^{13}\text{CO}(1-0)$ integrated intensity ($W_{[\text{CI}]} / W_{^{13}\text{CO}}$) distributions of RCW38 (Left: Ring cloud, Middle: Finger cloud) and declination-velocity diagram (Right). The black contours show the integrated intensity distribution and declination-velocity diagram of the [CI] emission. Contour levels of the Ring cloud are 3σ , 13σ , 23σ , 33σ , 43σ , 53σ , 63σ , 73σ , and 83σ ($1\sigma = 1.0 \text{ km s}^{-1}$). Contour levels of the Finger cloud are 3σ , 8σ , and 13σ ($1\sigma = 0.9 \text{ km s}^{-1}$). Contour levels of the declination-velocity diagram are 3σ , 8σ , 13σ , 18σ , 23σ , 28σ , 33σ , and 38σ ($1\sigma = 0.2 \text{ K}$). The vertical dashed lines indicate the integration range in the declination-velocity diagram. The black filled circles at the lower left corners show the HPBW of the [CI] and CO data ($40''$).

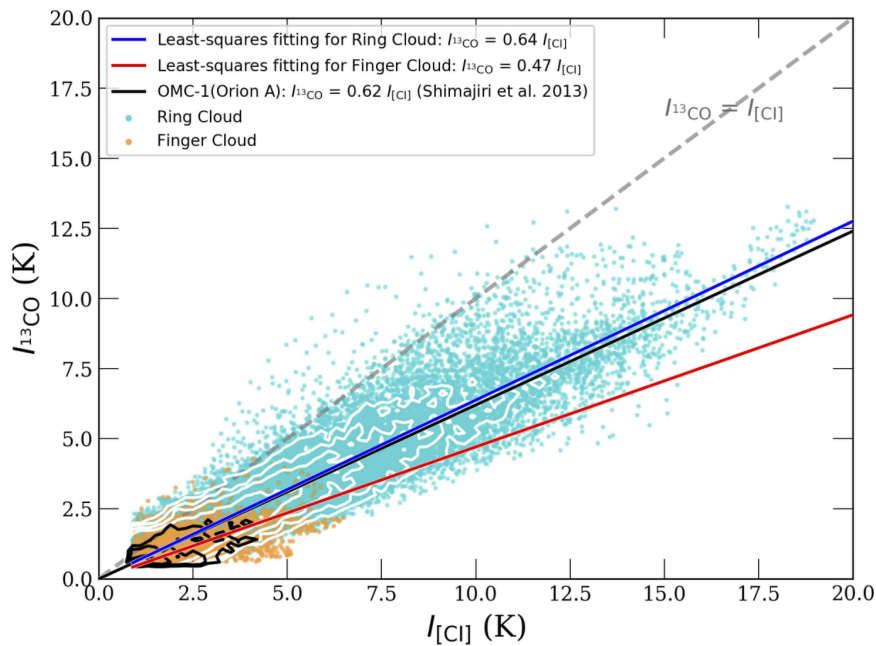


Fig. 5. Point-by-point correlations between [CI] and ^{13}CO (Cyan: Ring cloud, Orange: Finger cloud). Only pixels having intensities larger than the 3σ noise levels in the data cube are plotted. The 1σ noise levels of the [CI] and ^{13}CO are 0.3 and 0.2 K, respectively. The blue (Ring cloud) and red (Finger cloud) lines show the results of least-squares fitting: $I_{^{13}\text{CO}} = 0.64 (\pm 0.00066) \times I_{[\text{CI}]}$ and $I_{^{13}\text{CO}} = 0.47 (\pm 0.0043) \times I_{[\text{CI}]}$, respectively. The black line shows the result of least-squares fitting in the OMC-1 region in Orion A cloud: $I_{^{13}\text{CO}} = 0.62 \times I_{[\text{CI}]}$ (Shimajiri et al. 2013). The gray dotted-line represents $I_{^{13}\text{CO}} = I_{[\text{CI}]}$. The white and black contours show the distributions of all pixels for the Ring cloud and the Finger cloud, respectively (Ring cloud: 10, 20, 40, and 80 independent data points per 0.04 cell, Finger cloud: 10, 20, and 40 independent data points per 0.04 cell).

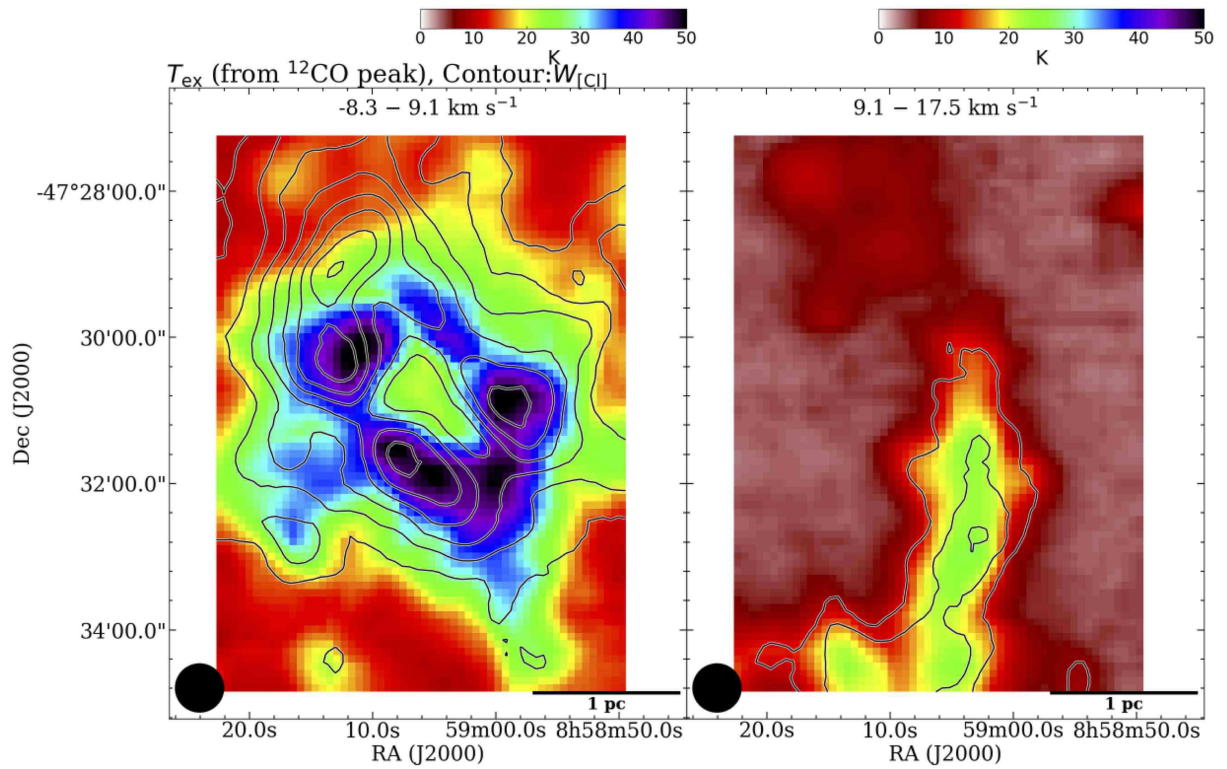


Fig. 6. Peak excitation temperature (T_{ex}) distribution of RCW38 derived from the peak intensity of $^{12}\text{CO}(1-0)$ data (Left: Ring cloud, Right: Finger cloud). The black contours show the integrated intensity distribution and declination-velocity diagram of [C I] emission. Contour levels of the Ring cloud are 3σ , 13σ , 23σ , 33σ , 43σ , 53σ , 63σ , 73σ , and 83σ ($1\sigma = 1.0 \text{ km s}^{-1}$). Contour levels of the Finger cloud are 3σ , 8σ , and 13σ ($1\sigma = 0.9 \text{ km s}^{-1}$). The black filled circles at the lower left corners show the HPBW of the [C I] and CO data ($40''$).

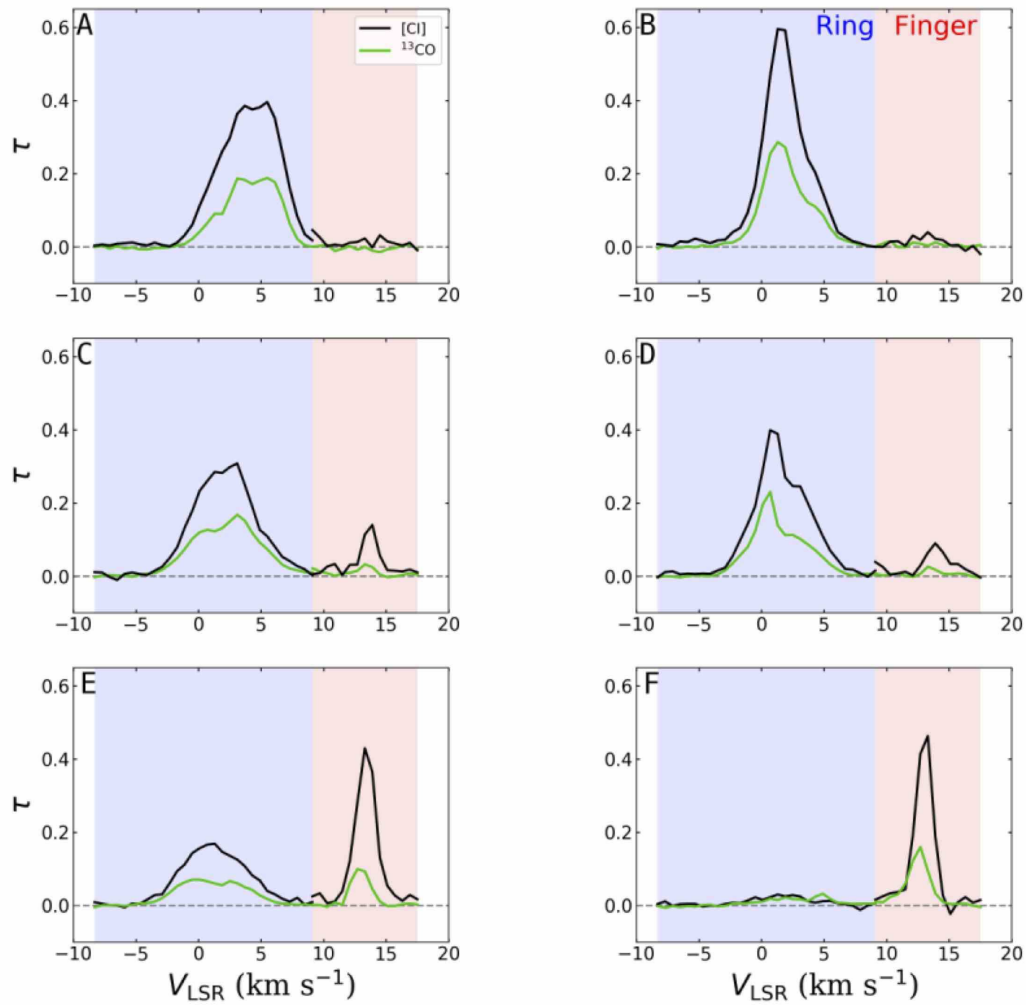


Fig. 7. Optical depth of [CI] (black lines) and $^{13}\text{CO}(1-0)$ (green lines) in the six [CI] peaks derived from the [CI] and $^{13}\text{CO}(1-0)$ spectra in Figure 3. These optical depths are derived with Eq. (6) by assuming that the excitation temperature for the Ring and Finger clouds are 49 K and 25 K, respectively. The blue and red areas indicate the velocity range of the Ring cloud (-8.3 – 9.1 km s^{-1}) and the Finger cloud (9.1 – 17.5 km s^{-1}), respectively.

Table 2. Properties of 6 [C I] peaks

Cloud	Name	T_{ex} (K)	$\overline{\tau}_{[\text{C I}]}$ *	$\overline{\tau}_{13\text{CO}}$	$N_{[\text{C I}]}$ (cm^{-2}) [†]	N_{CO} (cm^{-2})	$W_{[\text{C I}]} / W_{13\text{CO}}$	$N_{[\text{C I}]} / N_{\text{CO}}$
Ring	A	49	0.23	0.12	$1.2^{+0.3}_{-0.1} \times 10^{18}$	$9.5^{+5.3}_{-3.0} \times 10^{18}$	1.8 ± 0.1	$0.13^{+0.10}_{-0.05}$
	B	49	0.24	0.13	$1.2^{+0.5}_{-0.1} \times 10^{18}$	$1.0^{+0.6}_{-0.3} \times 10^{19}$	1.6 ± 0.1	$0.12^{+0.12}_{-0.05}$
	C	49	0.16	0.09	$9.4^{+1.5}_{-0.5} \times 10^{17}$	$9.0^{+5.3}_{-3.0} \times 10^{18}$	1.4 ± 0.1	$0.10^{+0.08}_{-0.04}$
	D	49	0.20	0.09	$9.1^{+1.6}_{-0.5} \times 10^{17}$	$8.0^{+4.6}_{-2.6} \times 10^{18}$	1.6 ± 0.1	$0.11^{+0.08}_{-0.05}$
	E	49	0.10	0.05	$5.3^{+0.7}_{-0.5} \times 10^{17}$	$4.2^{+2.8}_{-1.6} \times 10^{18}$	1.9 ± 0.2	$0.13^{+0.10}_{-0.06}$
	F	49	0.03	0.02	$3.4^{+1.3}_{-1.1} \times 10^{16}$	$9.0^{+7.8}_{-4.2} \times 10^{17}$	0.56 ± 0.2	$0.04^{+0.06}_{-0.02}$
Finger	A	25	—	—	—	—	—	—
	B	25	—	—	—	—	—	—
	C	25	0.13	0.03	$3.0^{+0.9}_{-0.6} \times 10^{16}$	$4.9^{+2.3}_{-1.9} \times 10^{16}$	5.3 ± 2.0	$0.61^{+0.69}_{-0.28}$
	D	25	0.07	—	$2.6^{+1.0}_{-0.8} \times 10^{16}$	—	—	—
	E	25	0.27	0.07	$1.6^{+0.4}_{-0.2} \times 10^{17}$	$4.5^{+1.3}_{-1.1} \times 10^{17}$	2.7 ± 0.4	$0.36^{+0.23}_{-0.11}$
	F	25	0.31	0.08	$1.5^{+0.4}_{-0.2} \times 10^{17}$	$7.6^{+2.0}_{-1.7} \times 10^{17}$	1.6 ± 0.2	$0.20^{+0.12}_{-0.06}$

* $\overline{\tau}$ denotes averaged optical depth. [†] Errors of column densities are derived by varying the assumed T_{ex} of the Ring and Finger clouds from 30 K to 80 K and from 20 K to 30 K, respectively.

Table 3. Average and standard deviation values of [C I]/CO ratio

Cloud	$W_{[\text{C I}]} / W_{13\text{CO}}$		$N_{[\text{C I}]} / N_{\text{CO}}$	
	average	standard deviation	average	standard deviation
Ring	1.5	0.35	0.11	0.026
Fing	2.4	0.69	0.29	0.084

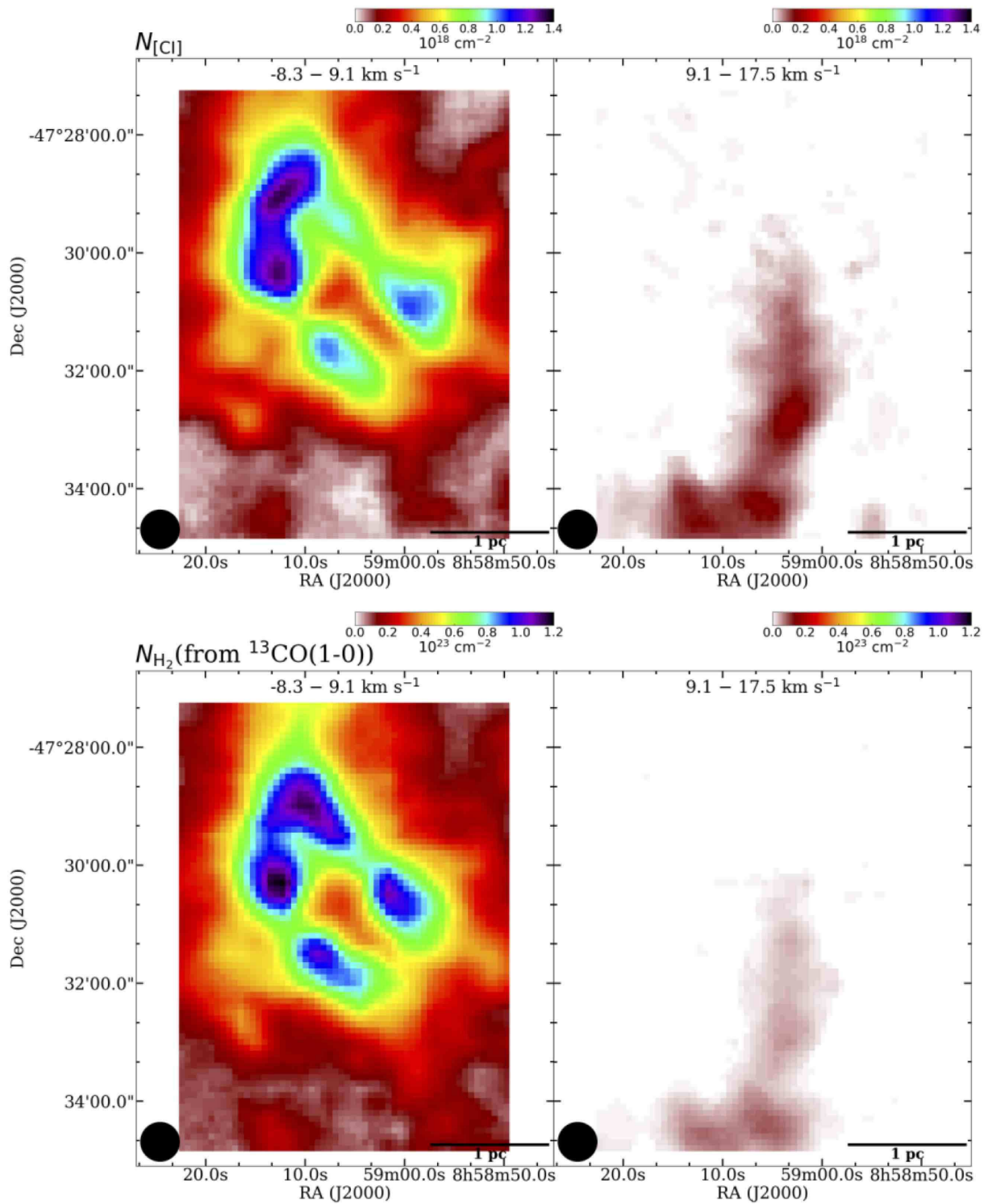


Fig. 8. [CI] (Top) and H₂ (Bottom) column density distributions of RCW38 (Left: Ring cloud, Right: Finger cloud). The black filled circles at the lower left corners show the HPBW of the [CI] and CO data (40').

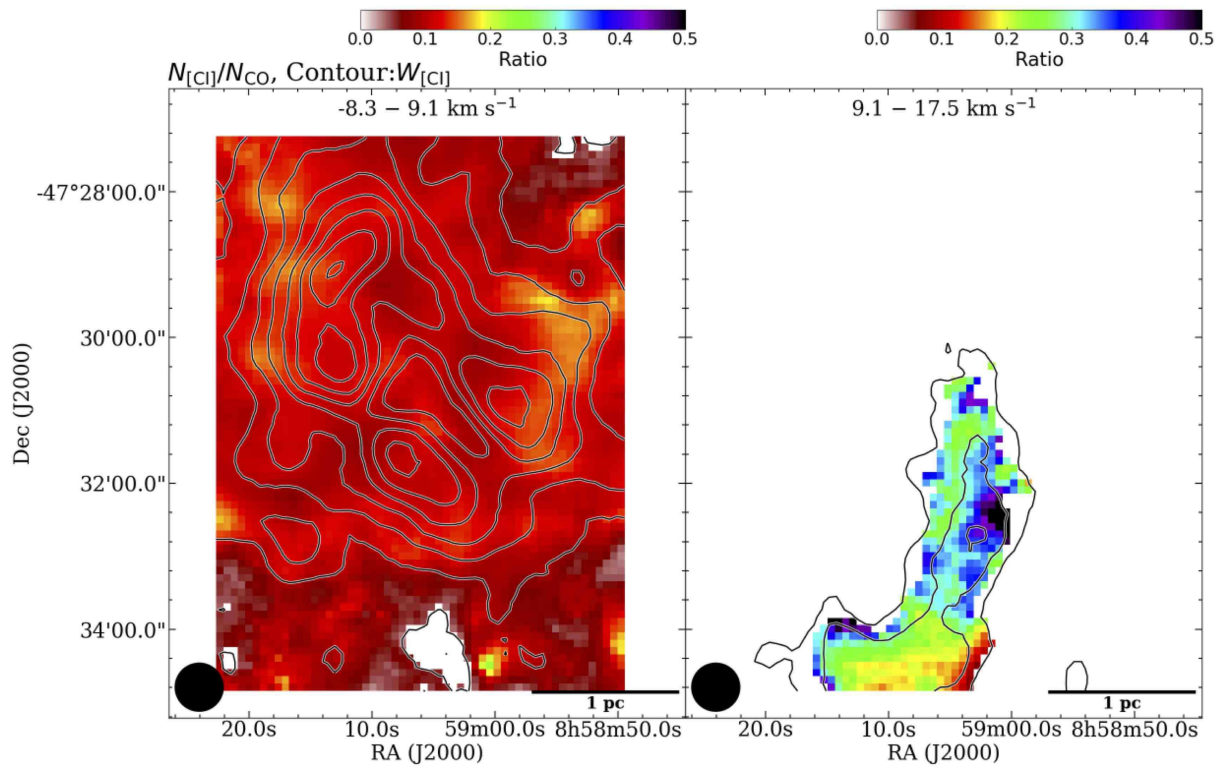


Fig. 9. Ratio of [C I]/CO column density ($N_{[\text{C I}]} / N_{\text{CO}}$) distribution of RCW38 (Left: Ring cloud, Right: Finger cloud). The black contours show the integrated intensity distribution of [C I] emission. Contour levels of the Ring cloud are 3σ , 13σ , 23σ , 33σ , 43σ , 53σ , 63σ , 73σ , and 83σ ($1\sigma = 1.0 \text{ km s}^{-1}$). Contour levels of the Finger cloud are 3σ , 8σ , and 13σ ($1\sigma = 0.9 \text{ km s}^{-1}$). The black filled circles at the lower left corners show the HPBW of the [C I] and CO data ($40''$).

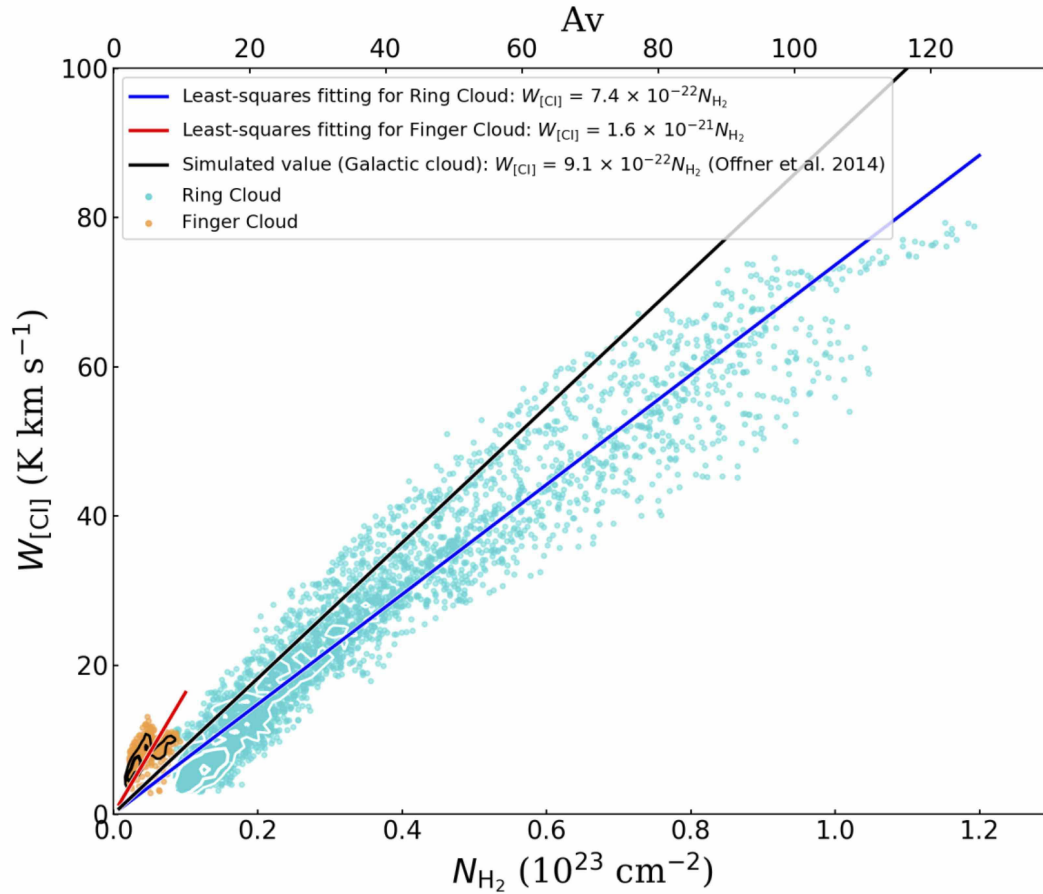


Fig. 10. Point-by-point correlations between the integrated intensity of [C I] emission and the H_2 column density (Cyan: Ring cloud, Orange: Finger cloud). Only pixels having intensities larger than the 3σ noise levels in the data are plotted. The 1σ noise levels of the [C I] integrated intensity and H_2 column density of the Ring cloud are 1.0 K km s^{-1} and $1.2 \times 10^{21} \text{ cm}^{-2}$, respectively. The 1σ noise levels of the [C I] integrated intensity and H_2 column density of the Finger cloud are 0.9 K km s^{-1} and $5.6 \times 10^{20} \text{ cm}^{-2}$, respectively. The blue and red lines show the results of least-squares fitting for the Ring cloud and the Finger cloud: $W_{[C I]} = 7.4 (\pm 0.02) \times 10^{-22} N_{H_2}$ and $W_{[C I]} = 1.6 (\pm 0.02) \times 10^{-21} N_{H_2}$, respectively. The black line shows the simulated value for a typical Galactic cloud: $W_{[C I]} = 9.1 \times 10^{-22} N_{H_2}$ by Offner et al. (2014). The white and black contours show the distributions of all pixels for the Ring cloud and the Finger cloud, respectively (Ring cloud: 10 and 20 independent data points per 1.5×10^{21} cell Finger cloud: 5 and 15 independent data points per 0.5×10^{21} cell).

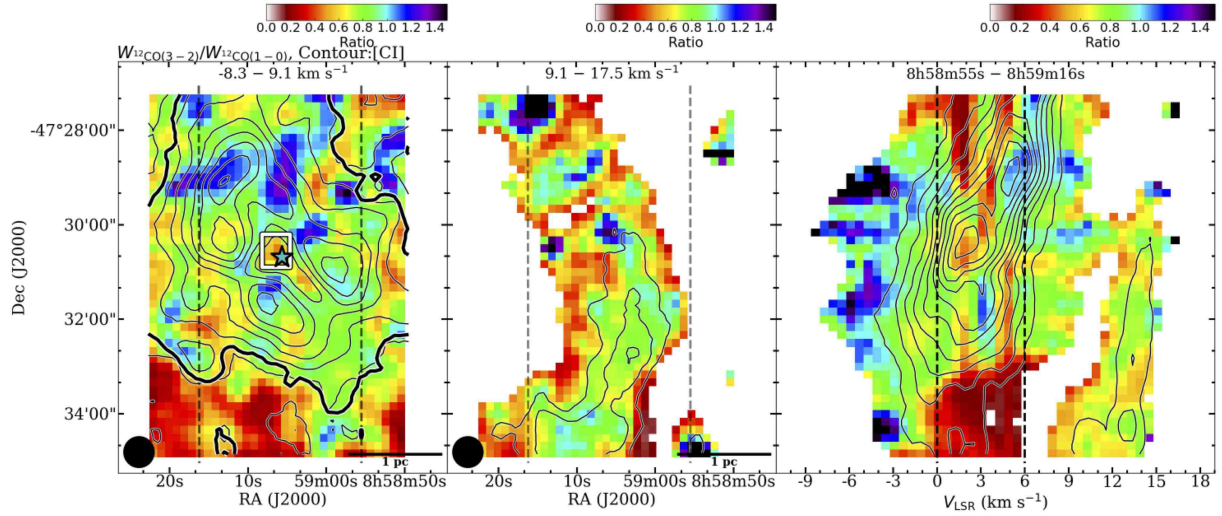


Fig. 11. Ratio of $^{12}\text{CO}(3-2)/^{12}\text{CO}(1-0)$ integrated intensity ($W_{12\text{CO}(3-2)}/W_{12\text{CO}(1-0)}$) distributions of RCW38 (Left: Ring cloud, Middle: Finger cloud) and declination-velocity diagram (Right). To remove the effect of the self-absorption, we except $v_{\text{LSR}} = 0.0\text{--}6.0\text{ km s}^{-1}$ component in the Left panel. The thin black contours show the integrated intensity distribution and declination-velocity diagram of [C I] emission. Contour levels of the Ring cloud are 3σ , 13σ , 23σ , 33σ , 43σ , 53σ , 63σ , 73σ , and 83σ ($1\sigma = 1.0\text{ km s}^{-1}$). Contour levels of the Finger cloud are 3σ , 8σ , and 13σ ($1\sigma = 0.9\text{ km s}^{-1}$). Contour levels of the declination-velocity diagram are 3σ , 8σ , 13σ , 18σ , 23σ , 28σ , 33σ , and 38σ ($1\sigma = 0.2\text{ K}$). The thick black contour in the left panel shows the 20σ value (2.0 km s^{-1}) of the $^{13}\text{CO}(1-0)$ integrated intensity. The white box in the left panel shows the inner region of the Ring cloud. The cyan star symbol indicates the peak of IRS 2. The vertical dashed lines in the Left and Middle panels indicate the integration range in the declination-velocity diagram. The black vertical dashed line in the Right panel indicates the region strongly affected by the self-absorption. The black filled circles at the lower left corners show the HPBW of the [C I] and CO data ($40''$).

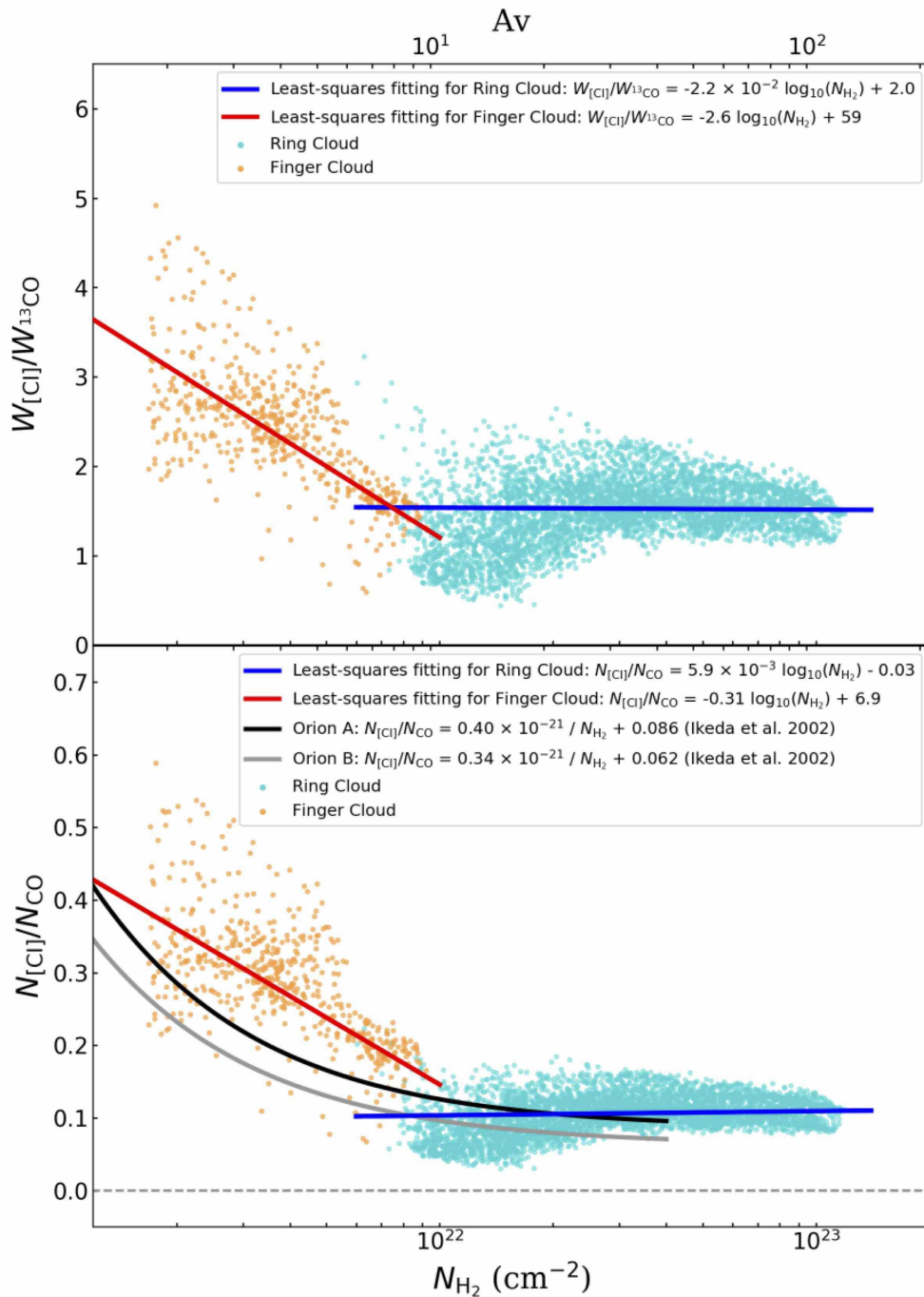


Fig. 12. Point-by-point correlations between the ratios of [CII]¹³CO integrated intensity (Top), [CII]/CO column density (Bottom), and H₂ column density (Cyan: Ring cloud, Orange: Finger cloud). Only pixels having intensities larger than the 3 σ noise levels in the data are plotted. The 1 σ noise levels of the [CII] column density, CO column density, H₂ column density, [CII] intensity, and ¹³CO intensity of the Ring cloud are $1.4 \times 10^{16} \text{ cm}^{-2}$, $1.2 \times 10^{17} \text{ cm}^{-2}$, $1.2 \times 10^{21} \text{ cm}^{-2}$, 1.0 K km s^{-1} , and 0.5 K km s^{-1} , respectively. The 1 σ noise levels of the [CII] column density, CO column density, H₂ column density, [CII] intensity, and ¹³CO intensity of the Finger cloud are $1.2 \times 10^{16} \text{ cm}^{-2}$, $5.6 \times 10^{16} \text{ cm}^{-2}$, $5.6 \times 10^{20} \text{ cm}^{-2}$, 0.9 K km s^{-1} , and 0.4 K km s^{-1} , respectively. The blue and red lines in the top panel show the results of least-squares fitting for the Ring cloud and the Finger cloud: $R_{[CII]/^{13}\text{CO}} = -2.2 (\pm 1.6) \times 10^{-2} \log_{10}(N_{\text{H}_2}) + 2.0$ and $R_{[CII]/^{13}\text{CO}} = -2.6 (\pm 0.1) \log_{10}(N_{\text{H}_2}) + 59 (\pm 2)$, respectively. The blue and red lines in the bottom panel show the results of least-squares fitting for the Ring cloud and the Finger cloud: $N_{[CII]}/N_{^{13}\text{CO}} = 5.9 (\pm 1.2) \times 10^{-3} \log_{10}(N_{\text{H}_2}) - 0.03 (\pm 0.03)$ and $N_{[CII]}/N_{^{13}\text{CO}} = -0.47 (\pm 0.02) \log_{10}(N_{\text{H}_2}) + 10 (\pm 0.4)$, respectively. The black and gray lines in the bottom panel show the results of least-squares fitting for Orion A and B clouds, respectively (Ikeda et al. 2002).

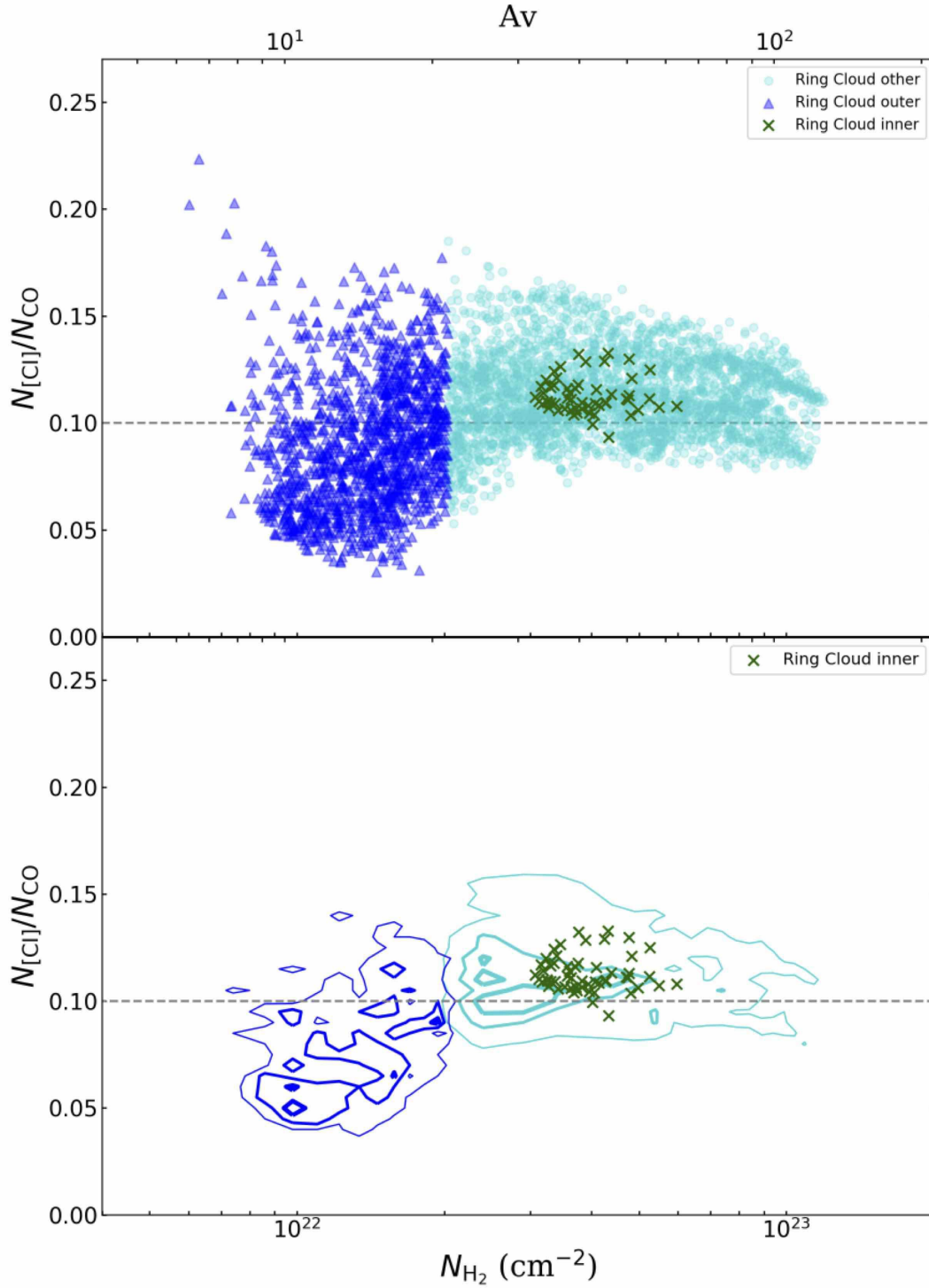


Fig. 13. Point-by-point correlations between the ratio of [C]I/CO column density and H_2 column density for the Ring cloud. Top panel: blue, green, and cyan points show the outer, inner, and the other regions in the Ring cloud, respectively. Bottom panel: cyan and blue contours show the distributions of all pixels for the other region and the outer region in the Ring cloud, respectively (Other region: 6, 18, and 30 independent data points per 2.5×10^{19} (5.0×10^{21}) \times 0.005) cell, Outer region: 4, 9, and 14 independent data points per 0.6×10^{19} (1.2×10^{21}) \times 0.005) cell).

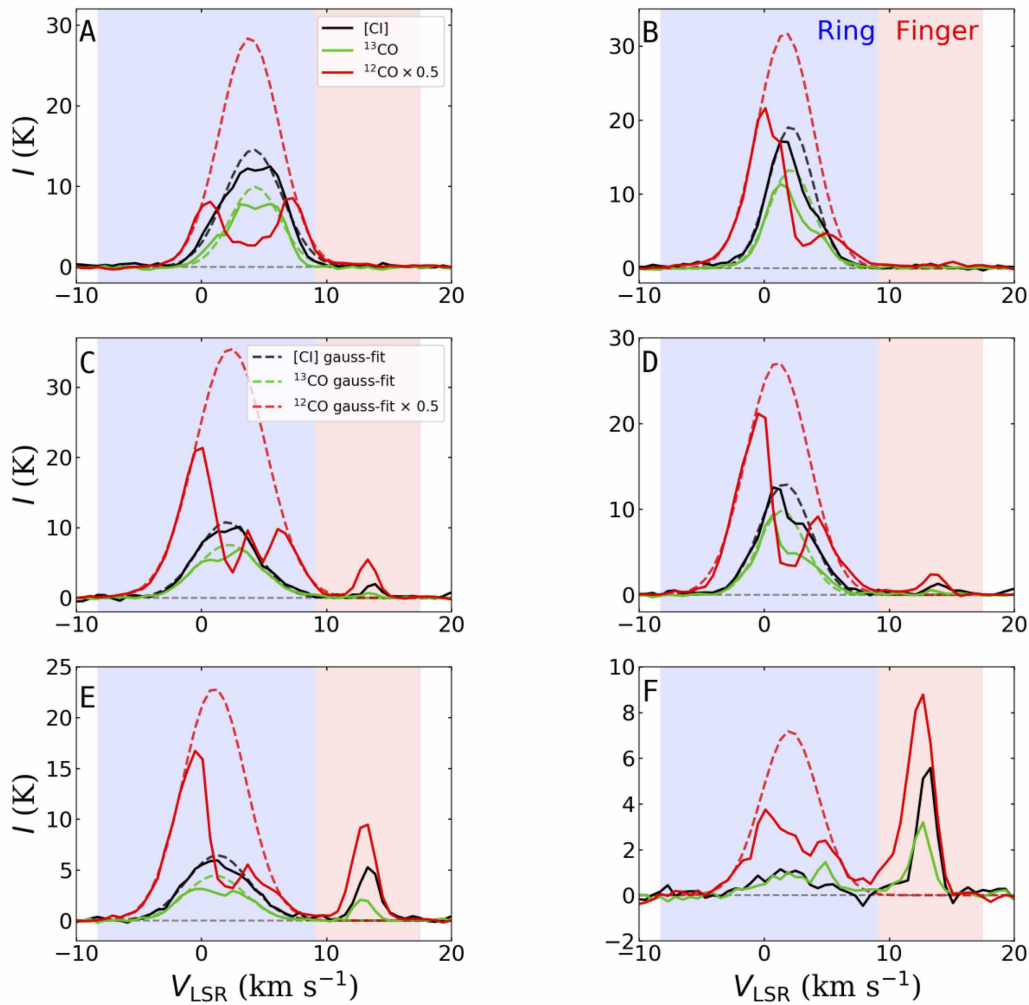


Fig. 14. Detected spectra (solid lines, same as in the Figure 3) and gaussian-fitted spectra (dashed lines, only for the Ring cloud) of the [C I], ^{13}CO , and ^{12}CO emissions for the six [C I] peaks. The blue and red areas indicate the velocity range of the Ring cloud (-8.3 – 9.1 km s^{-1}) and the Finger cloud (9.1 – 17.5 km s^{-1}), respectively. We did not fit gaussian function to [C I] and ^{13}CO spectra of peak F because we could not detect any self-absorption feature of [C I] and ^{13}CO emission in the peak.

Acknowledgments

We are grateful to the ASTE staff for operating the ASTE and helping us with data reduction. We would like to thank Hauyu Baobab Liu for helpful discussions. We also would like to thank the anonymous referee for a careful reading and thoughtful suggestions that significantly improved this paper. This work is supported by JSPS KAKENHI Grant Nos. 15H02074 and 18H05441.

References

- Burton, M. G., Ashley, M. C. B., Braiding, C., et al. 2015, *ApJ*, 811, 13
- Clark, P. C., Glover, S. C. O., Ragan, S. E., et al. 2019, *MNRAS*, 486, 4622
- DeRose, K. L., Bourke, T. L., Gutermuth, R. A., et al. 2009, *AJ*, 138, 33.
- Emerson, D. T., & Graeve, R. 1988, *A&A*, 190, 353
- Ezawa, H., Kawabe, R., Kohno, K., & Yamamoto, S. 2004, *Proc. SPIE*, 5489, 763
- Ferland, G. J., Korista, K. T., Verner, D. A., et al. 1998, *PASP*, 110, 761.
- Frerking, M. A., Langer, W. D., & Wilson, R. W. 1982, *ApJ*, 262, 590
- Frogel, J. A., & Persson, S. E. 1974, *ApJ*, 192, 351.
- Furniss, I., Jennings, R. E., & Moorwood, A. F. M. 1975, *ApJ*, 202, 400.
- Fukui, Y., Torii, K., Ohama, A., et al. 2016, *ApJ*, 820, 26
- Fukui, Y., Hayakawa, T., Inoue, T., et al. 2018, *ApJ*, 860, 33.
- Fukui, Y., Inoue, T., Hayakawa, T., et al. 2019, arXiv e-prints, arXiv:1909.08202
- Glover, S. C. O., Clark, P. C., Micic, M., et al. 2015, *MNRAS*, 448, 1607.
- Goldreich, P., & Kwan, J. 1974, *ApJ*, 189, 441.
- Gyulbudaghian, A. L., & May, J. 2008, *Astrophysics*, 51, 18.
- Hollenbach, D. J., Takahashi, T., & Tielens, A. G. G. M. 1991, *ApJ*, 377, 192
- Hollenbach, D. J., & Tielens, A. G. G. M. 1997, *ARA&A*, 35, 179
- Hollenbach, D. J., & Tielens, A. G. G. M. 1999, *Reviews of Modern Physics*, 71, 173
- Ikeda, M., Ohishi, M., Nummelin, A., et al. 2002, *ApJ*, 571, 560
- Inoue, T., & Fukui, Y. 2013, *ApJL*, 774, L31
- Ito, T., Kamazaki, T., Fujii, Y., et al. 2018, *Millimeter, Submillimeter, and Far-Infrared Detectors and Instrumentation for Astronomy IX*, 10708, 107082V
- Kamazaki, T., Ezawa, H., Tatematsu, K., et al. 2005, *Astronomical Data Analysis Software and Systems XIV*, 347, 533
- Kohno, K., Yamamoto, S., Kawabe, R., et al. 2004, *The Dense Interstellar Medium in Galaxies*, 91, 349
- Kramer, C., Cubick, M., Röllig, M., et al. 2008, *A&A*, 477, 547
- Leung, C. M., Herbst, E., & Huebner, W. F. 1984, *ApJS*, 56, 231
- Mangum, J. G., Emerson, D. T., & Greisen, E. W. 2007, *A&A*, 474, 679
- Mangum, J. G., & Shirley, Y. L. 2015, *PASP*, 127, 266
- McMullin, J. P., Waters, B., Schiebel, D., Young, W., & Golap, K. 2007, *Astronomical Data Analysis Software and Systems XVI*, 376, 127
- Mizuno, A., Onishi, T., Yonekura, Y., et al. 1995, *ApJL*, 445, L161
- Offner, S. S. R., Bisbas, T. G., Bell, T. A., et al. 2014, *MNRAS*, 440, L81
- Oka, T., Yamamoto, S., Iwata, M., et al. 2001, *ApJ*, 558, 176
- Oka, T., Kamegai, K., Hayashida, M., et al. 2005, *ApJ*, 623, 889
- Phillips, T. G., Huggins, P. J., Kuiper, T. B. H., et al. 1980, *ApJL*, 238, L103
- Rodgers, A. W., Campbell, C. T., & Whiteoak, J. B. 1960, *MNRAS*, 121, 103
- Röllig, M., Abel, N. P., Bell, T., et al. 2007, *A&A*, 467, 187.
- Sawada, T., Ikeda, N., Sunada, K., et al. 2008, *PASJ*, 60, 445
- Shimajiri, Y., Sakai, T., Tsukagoshi, T., et al. 2013, *ApJL*, 774, L20
- Smith, C. H., Bourke, T. L., Wright, C. M., et al. 1999, *MNRAS*, 303, 367
- Sorai, K., Sunada, K., Okumura, S. K., et al. 2000, *Proc. SPIE*, 4015, 86
- Szűcs, L., Glover, S. C. O., & Klessen, R. S. 2014, *MNRAS*, 445, 4055. doi:10.1093/mnras/stu2013
- Tachihara, K., Fukui, Y., Hayakawa, T., et al. 2018, arXiv e-prints, arXiv:1811.02224.
- Tielens, A. G. G. M., & Hollenbach, D. 1985, *ApJ*, 291, 747
- Torii, K., Tokuda, K., Tachihara, K., et al. 2019, arXiv e-prints, arXiv:1907.07358
- van Dishoeck, E. F., & Black, J. H. 1988, *ApJ*, 334, 771
- Warin, S., Benayoun, J. J., & Viala, Y. P. 1996, *A&A*, 308, 535
- Wilson, T. L., & Rood, R. 1994, *ARA&A*, 32, 191
- Winston, E., Wolk, S. J., Bourke, T. L., et al. 2011, *ApJ*, 743, 166
- Wolk, S. J., Spitzbart, B. D., Bourke, T. L., & Alves, J. 2006, *AJ*, 132, 1100
- Wolk, S. J., Bourke, T. L., & Vigil, M. 2008, *Handbook of Star Forming Regions, Volume II*, 5, 124
- Yamaguchi, R., Saito, H., Mizuno, N., et al. 1999, *PASJ*, 51, 791.
- Zinchenko, I., Mattila, K., & Toriseva, M. 1995, *A&AS*, 111, 95.

Appendix 1 Velocity-channel distributions of RCW38

Velocity-channel distributions of RCW38 are shown in this appendix. Figure 15 and Figure 16 show the velocity-channel map of [CI] emission and [CI] / ^{13}CO intensity ratio, respectively, for every 2.4 km s^{-1} .

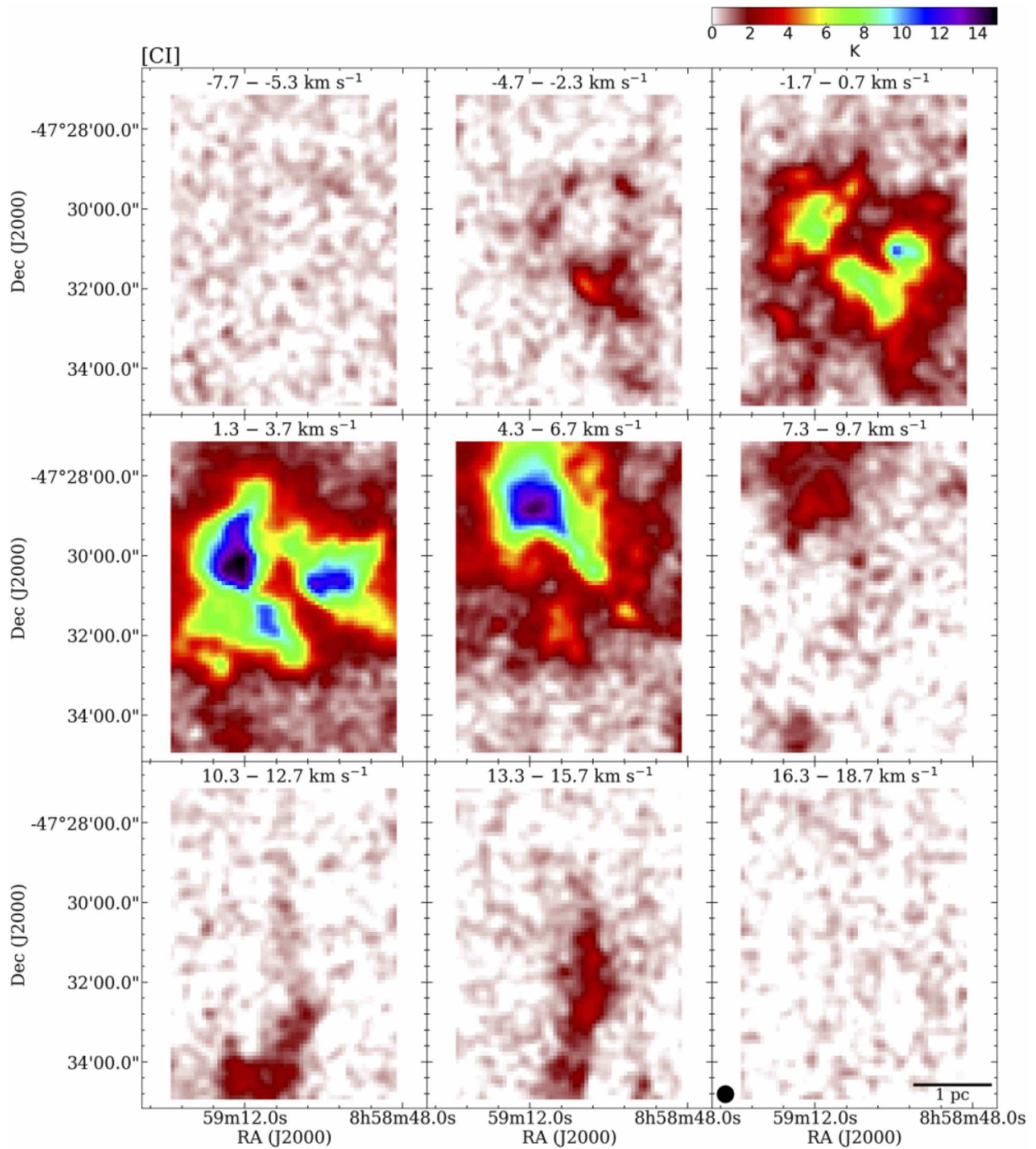


Fig. 15. [CI] velocity-channel map of RCW38. These data were smoothed to an HPBW of $26''$ with a 2D Gaussian function, and the rms noise level was reduced to a typical value of 0.5 K in T_{MB} . The black filled circle at the lower left corner in the bottom right panel shows the HPBW size.

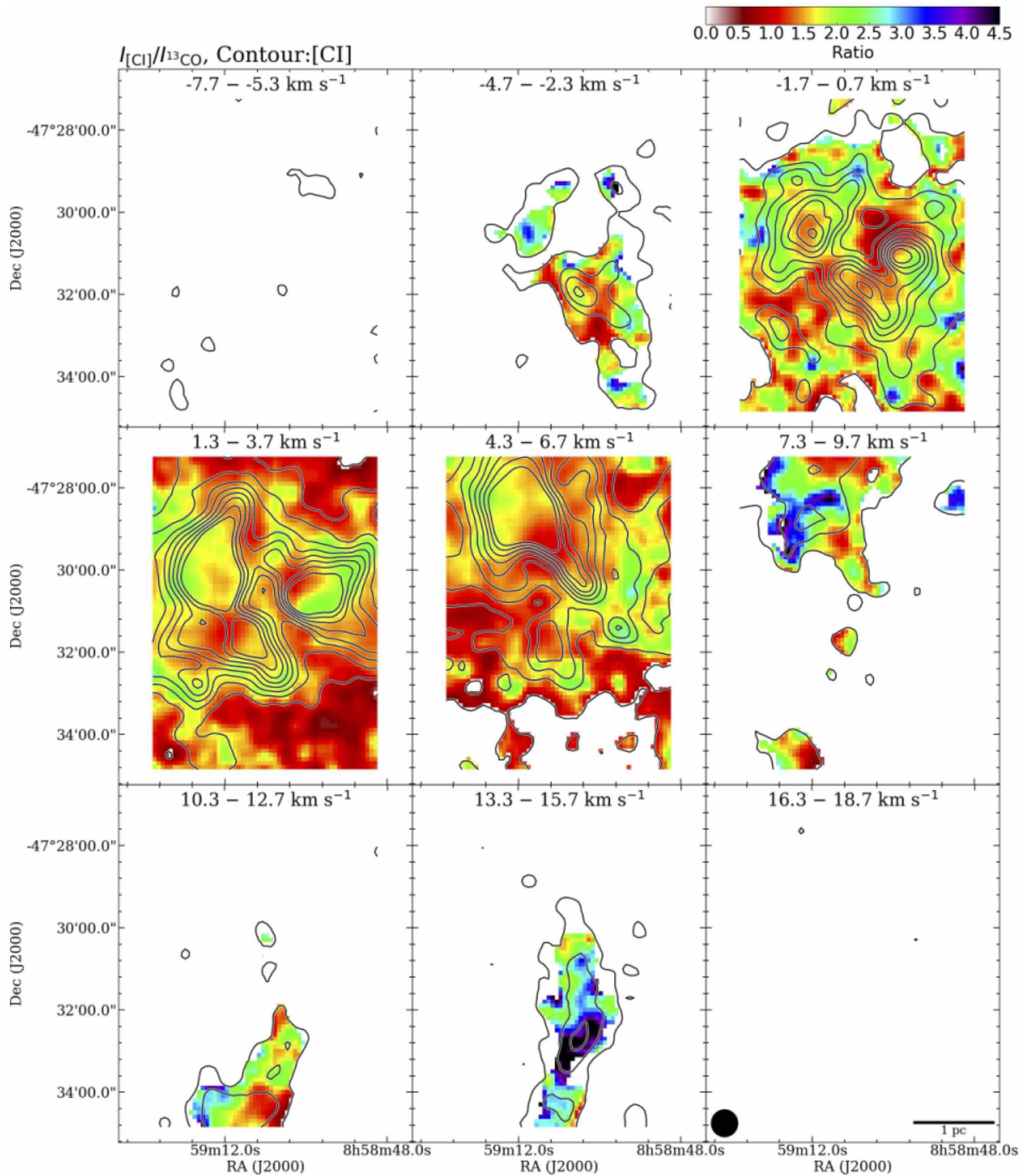


Fig. 16. Ratio of [C I] / ¹³CO line velocity-channel map of RCW38. The black contours show the [C I] distribution (Contour levels: 3σ, 5σ, 13σ, 18σ, 23σ, 28σ, 33σ, 38σ, and 43σ, 1σ = 0.2 K). The black filled circle at the lower left corner in the bottom right panel shows the HPBW of the [C I] and CO data (40'').

Appendix 2 Results using T_{ex} derived from peak intensity of the $^{12}\text{CO}(1-0)$

In Sections 3 and 4, we presented the results in which T_{ex} was assumed to be uniform in both the Ring and the Finger clouds. To assess the possible effects by variation of T_{ex} , we present the results of [CI] parameters by employing a non-uniform distribution of T_{ex} . The results confirm that the present results of the [CI]/CO abundance ratio are robust. To note, we did not calculate the column densities in the region with the ratio of $^{13}\text{CO}(1-0)/^{12}\text{CO}(1-0)$ peak intensity of more than 1/3, which corresponds to $\tau_{^{13}\text{CO}}$ of more than ~ 0.4 estimated from the following equation:

$$\frac{T_{\text{MB}}(^{12}\text{CO})}{T_{\text{MB}}(^{13}\text{CO})} = \frac{1 - e^{-\tau_{^{12}\text{CO}}}}{1 - e^{-\tau_{^{13}\text{CO}}}}. \quad (\text{A1})$$

and from the assumption that the abundance ratio of $^{12}\text{CO}/^{13}\text{CO}$ is 77 (Wilson & Rood 1994). This is because the region is considered to be strongly affected by self-absorption (uncertainty of T_{ex} in this region is considered to be very large).

Figure 17 shows the [CI] (top) and H_2 (bottom) column density distributions of RCW38. The [CI] column densities of the Ring and Finger clouds are $(0.1\text{--}1.3) \times 10^{18}$ and $(0.1\text{--}0.2) \times 10^{18} \text{ cm}^{-2}$, respectively. The H_2 column densities of the Ring and Finger clouds are $(0.1\text{--}1.0) \times 10^{23}$ and $\sim 0.1 \times 10^{23} \text{ cm}^{-2}$, respectively. Figure 18 shows the distribution of the ratio of [CI]/CO column density ($N_{[\text{CI}]} / N_{\text{CO}}$) of RCW38. The ratio in both the Ring and Finger clouds are 0.1–0.6. Figure 19 shows the relationship between [CI] integrated intensity ($W_{[\text{CI}]}$) and H_2 column density (N_{H_2}). The conversion factors from $W_{[\text{CI}]}$ to N_{H_2} ($X_{[\text{CI}]} = N_{\text{H}_2} / W_{[\text{CI}]}$) for the Ring and Finger clouds are $X_{[\text{CI}]} = 1.1 (\pm 0.005) \times 10^{21} \text{ cm}^{-2} \text{ K}^{-1} \text{ km}^{-1} \text{ s}$ (corresponding to $W_{[\text{CI}]} = 9.0 (\pm 0.04) \times 10^{-22} N_{\text{H}_2}$) and $X_{[\text{CI}]} = 5.6 (\pm 0.09) \times 10^{20} \text{ cm}^{-2} \text{ K}^{-1} \text{ km}^{-1} \text{ s}$ (corresponding to $W_{[\text{CI}]} = 1.8 (\pm 0.03) \times 10^{-22} N_{\text{H}_2}$), respectively.

The top panel in Figure 20 shows the relationship between $W_{[\text{CI}]} / W_{^{13}\text{CO}}$ and N_{H_2} , and the bottom panel in Figure 12 shows the relationship between $N_{[\text{CI}]} / N_{\text{CO}}$ and N_{H_2} . In the low- A_V region ($A_V \leq 10$ mag), $W_{[\text{CI}]} / W_{^{13}\text{CO}}$ decreases with A_V from ~ 5 to ~ 1 . In the high- A_V region ($A_V > 10$ mag), $W_{[\text{CI}]} / W_{^{13}\text{CO}}$ is almost constant (~ 1.5) for A_V of up to 100 mag. A similar trend is seen in the relationship between $N_{[\text{CI}]} / N_{\text{CO}}$ and A_V (N_{H_2}). In the low- A_V region ($A_V \leq 10$ mag), $N_{[\text{CI}]} / N_{\text{CO}}$ decreases with A_V from ~ 1.6 to ~ 0.2 . In the high- A_V region ($A_V > 10$ mag), $N_{[\text{CI}]} / N_{\text{CO}}$ gradually decreases with A_V from ~ 1.2 to ~ 0.1 and $N_{[\text{CI}]} / N_{\text{CO}}$ is ~ 0.1 for A_V of up to 100 mag.

Figure 21 shows the relationship between $N_{[\text{CI}]} / N_{\text{CO}}$ and N_{H_2} for the inner, outer, and other regions of the Ring cloud. The ratio of $N_{[\text{CI}]} / N_{\text{CO}}$ in the inner region is

relatively larger than that in the other region. The ratio of $N_{[\text{CI}]} / N_{\text{CO}}$ in the outer region is slightly lower than that in the other region, especially for N_{H_2} of $\sim 10^{22} \text{ cm}^{-2}$.

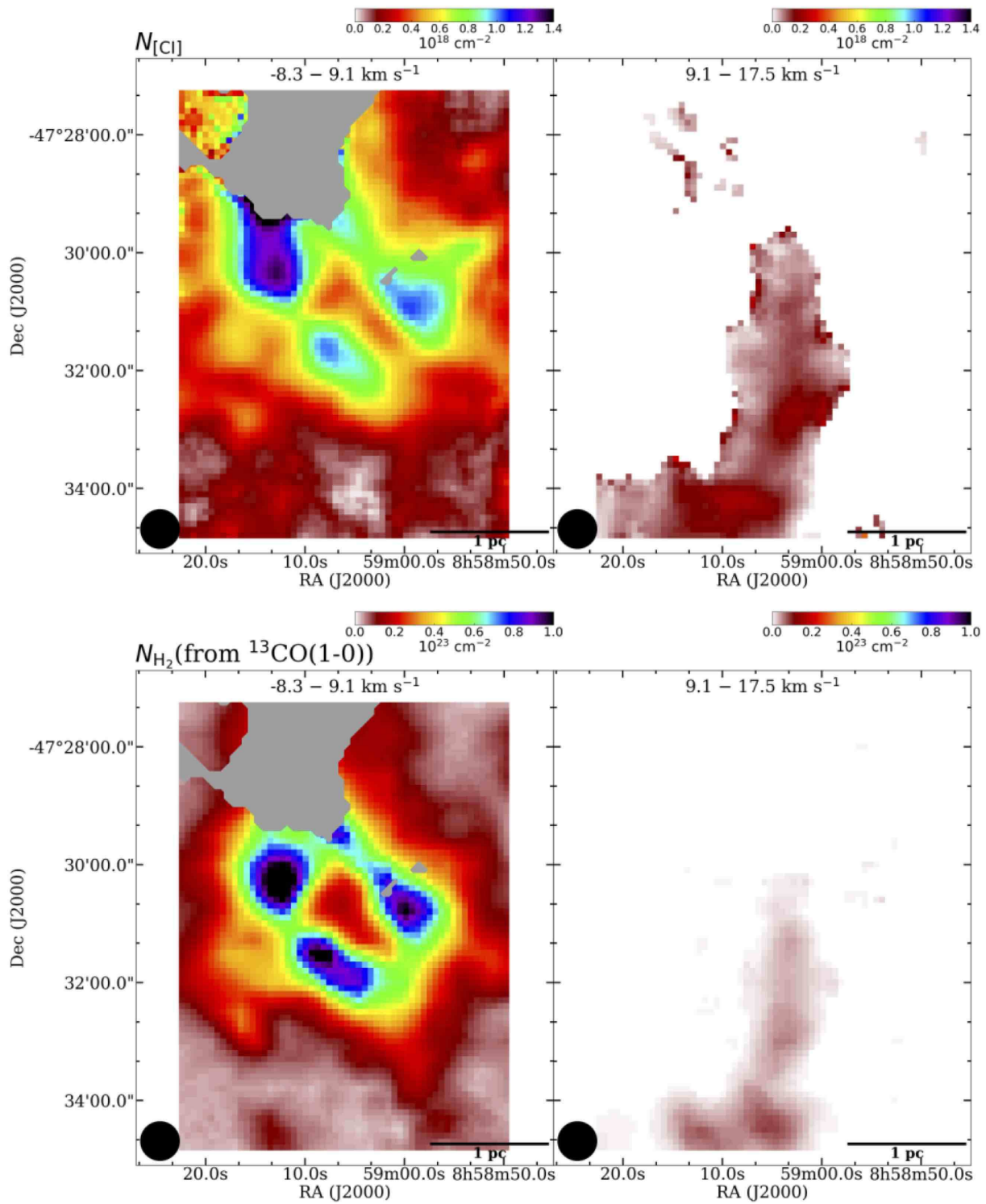


Fig. 17. [C I] (Top) and H₂ (Bottom) column density distributions of RCW38 (Left: Ring cloud, Right: Finger cloud) using T_{ex} derived from the peak intensity of the $^{12}\text{CO}(1-0)$. The gray regions in the Ring cloud indicate the masked region derived from the ratio of $^{13}\text{CO}(1-0) / ^{12}\text{CO}(1-0)$ peak intensity. The black filled circles at the lower left corners show the HPBW of the [C I] and CO data (40'').

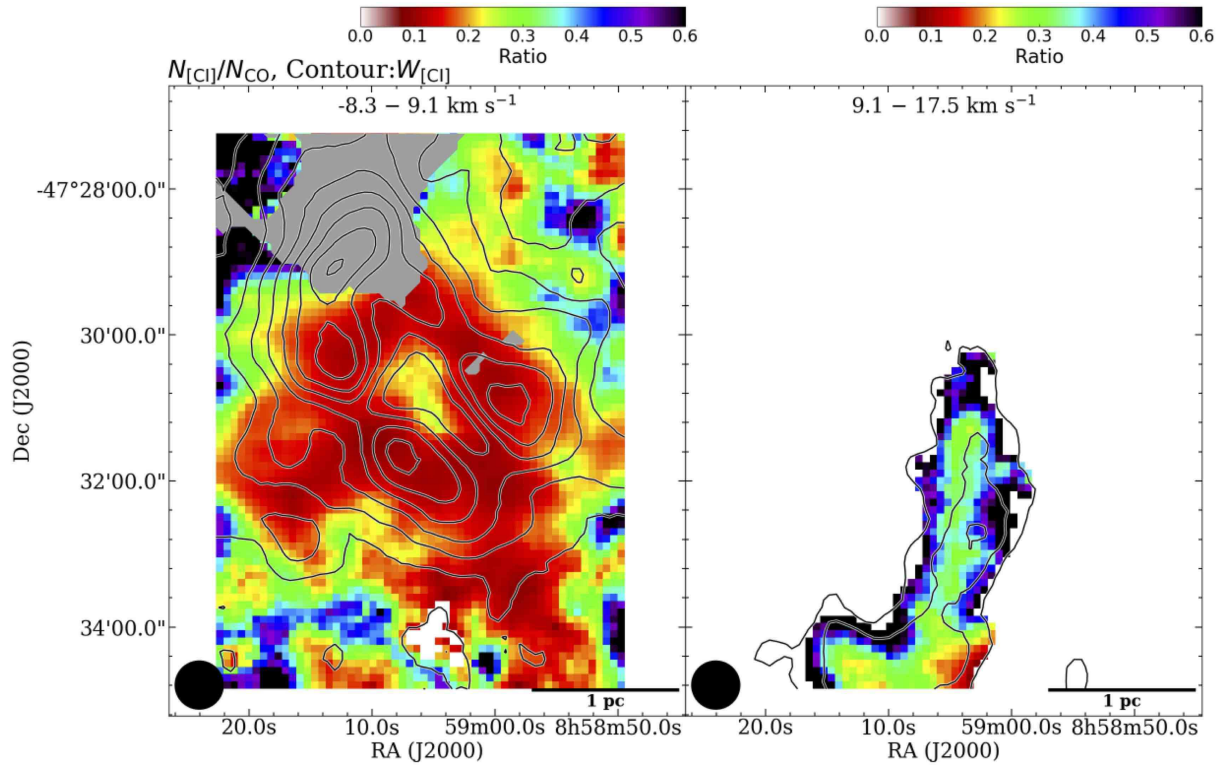


Fig. 18. Ratio of [C I]/CO column density ($N_{[C I]}/N_{CO}$) distribution of RCW38 (Left: Ring cloud, Right: Finger cloud) using T_{ex} derived from the peak intensity of the $^{12}\text{CO}(1-0)$. The black contours show the integrated intensity distribution of [C I] emission. Contour levels of the Ring cloud are 3σ , 13σ , 23σ , 33σ , 43σ , 53σ , 63σ , 73σ , and 83σ ($1\sigma = 1.0 \text{ km s}^{-1}$). Contour levels of the Finger cloud are 3σ , 8σ , and 13σ ($1\sigma = 0.9 \text{ km s}^{-1}$). The gray regions in the Ring cloud indicate the masked region derived from the ratio of $^{13}\text{CO}(1-0) / ^{12}\text{CO}(1-0)$ peak intensity. The black filled circles at the lower left corners show the HPBW of the [C I] and CO data ($40''$).

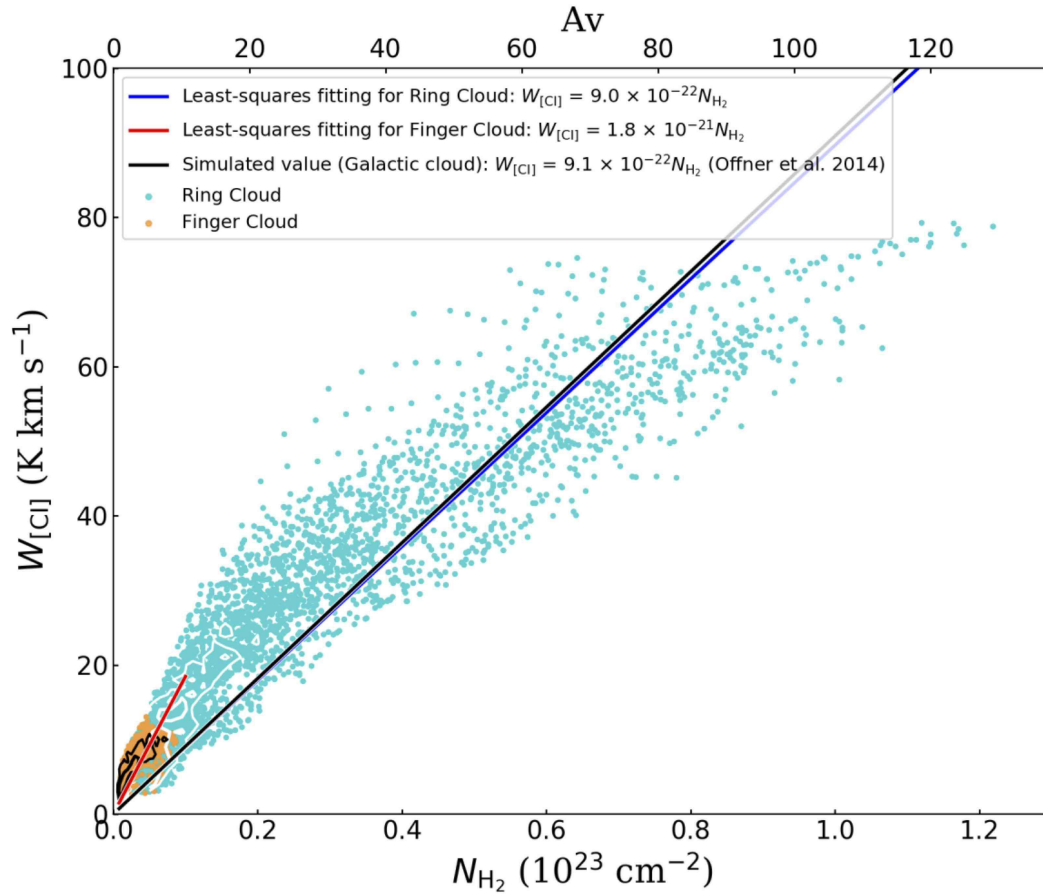


Fig. 19. Point-by-point correlations between the integrated intensity of [C I] emission and H_2 column density using T_{ex} derived from the peak intensity of the $^{12}\text{CO}(1-0)$ (Cyan: Ring cloud, Orange: Finger cloud). Only pixels having intensities larger than the 3σ noise levels in the data are plotted. The 1σ noise level of the [C I] integrated intensity and H_2 column density of the Ring cloud are 1.0 K km s^{-1} and $7.0 \times 10^{20} \text{ cm}^{-2}$, respectively, and those of the Finger cloud are 0.9 K km s^{-1} and $3.0 \times 10^{20} \text{ cm}^{-2}$, respectively. The blue and red lines show the results of the least-squares fitting for the Ring cloud and the Finger cloud: $W_{[C I]} = 9.0 (\pm 0.04) \times 10^{-22} N_{\text{H}_2}$ and $W_{[C I]} = 1.8 (\pm 0.03) \times 10^{-21} N_{\text{H}_2}$, respectively. The black line shows the simulated value for a typical Galactic cloud: $W_{[C I]} = 9.1 \times 10^{-22} N_{\text{H}_2}$ (Offner et al. 2014). The white and black contours show the distributions of all pixels for the Ring cloud and the Finger cloud, respectively (Ring cloud: 10 and 20 independent data points per 1.5×10^{21} cell, Finger cloud: 5 and 15 independent data points per 0.5×10^{21} cell).

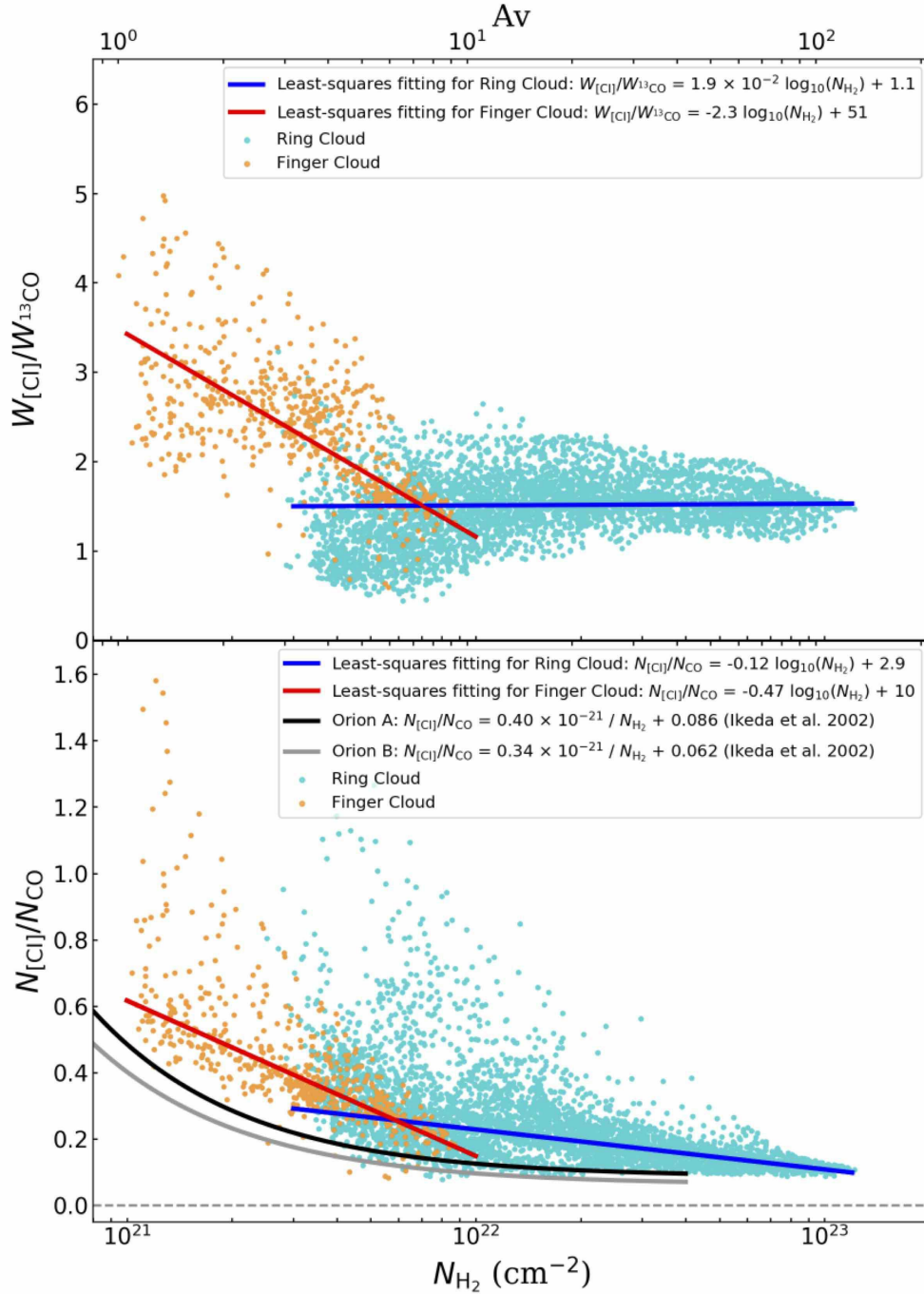


Fig. 20. Point-by-point correlations between the ratio of [CI] ^{13}CO integrated intensity (Top), [CI]/CO column density (Bottom), and H_2 column density (Cyan: Ring cloud, Orange: Finger cloud) using T_{ex} derived from the peak intensity of the $^{12}\text{CO}(1-0)$. Only pixels having intensities larger than the 3σ noise levels in the data are plotted. The 1σ noise levels of the [CI] column density, CO column density, H_2 column density, [CI] intensity, and ^{13}CO intensity of the Ring cloud are $1.8 \times 10^{16} \text{ cm}^{-2}$, $7.0 \times 10^{16} \text{ cm}^{-2}$, $7.0 \times 10^{20} \text{ cm}^{-2}$, 1.0 K km s^{-1} , and 0.5 K km s^{-1} , respectively. The 1σ noise levels of the [CI] column density, CO column density, H_2 column density, [CI] intensity, and ^{13}CO intensity of the Finger cloud are $1.2 \times 10^{16} \text{ cm}^{-2}$, $3.0 \times 10^{16} \text{ cm}^{-2}$, $3.0 \times 10^{20} \text{ cm}^{-2}$, 0.9 K km s^{-1} , and 0.4 K km s^{-1} , respectively. The blue and red lines in the top panel show the results of the least-squares fitting for the Ring cloud and the Finger cloud: $R_{[\text{CI}]/^{13}\text{CO}} = 1.9 (\pm 1.2) \times 10^{-2} \log_{10}(N_{\text{H}_2}) + 1.1 (\pm 0.3)$ and $R_{[\text{CI}]/^{13}\text{CO}} = -2.3 (\pm 0.1) \log_{10}(N_{\text{H}_2}) + 51 (\pm 2)$, respectively. The blue and red lines in the bottom panel show the results of the least-squares fitting for the Ring cloud and the Finger cloud: $N_{[\text{CI}]} / N_{^{13}\text{CO}} = -0.12 (\pm 0.002) \log_{10}(N_{\text{H}_2}) + 2.9 (\pm 0.05)$ and $N_{[\text{CI}]} / N_{^{13}\text{CO}} = -0.47 (\pm 0.02) \log_{10}(N_{\text{H}_2}) + 10 (\pm 0.4)$, respectively. The black and gray lines in the bottom panel show the results of least-squares fitting for the Orion A and B clouds, respectively (Ikeda et al. 2002).

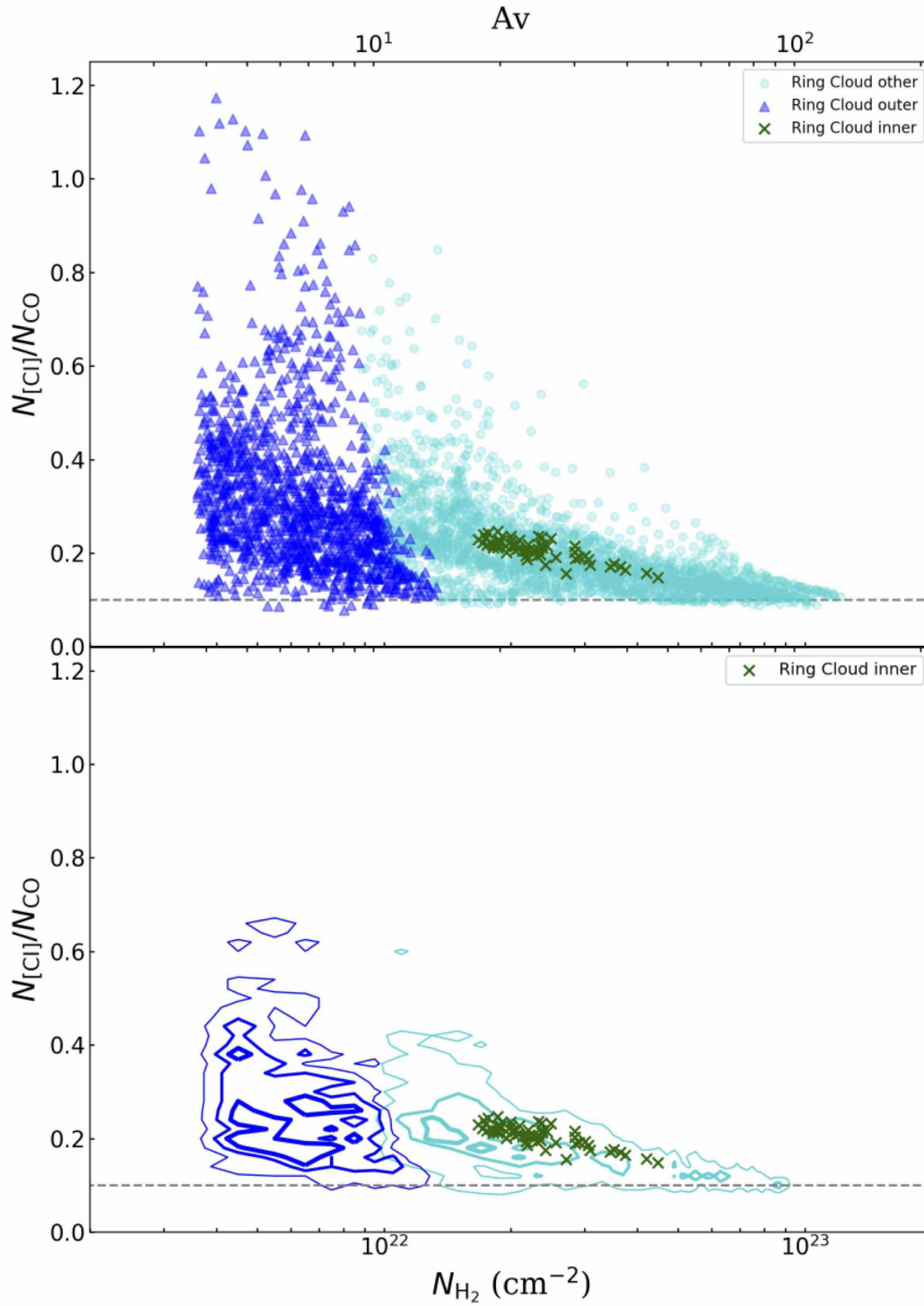


Fig. 21. Point-by-point correlations between the ratio of [CII]/CO column density and the H_2 column density for the Ring cloud using T_{ex} derived from the peak intensity of the $^{12}CO(1-0)$. Top panel: blue, green, and cyan points show the outer, inner, and the other regions in the Ring cloud, respectively. Bottom panel: cyan and blue contours show the distributions of all pixels for the other region and the outer region in the Ring cloud, respectively (Other region: 4, 12, and 20 independent data points per 4.0×10^{19} ($(2.0 \times 10^{21}) \times 0.02$) cell, Outer region: 3, 8, and 13 independent data points per 2.0×10^{19} ($(1.0 \times 10^{21}) \times 0.02$) cell).